



HAL
open science

Fossil field decay due to nonlinear tides in massive binaries

Jérémie Vidal, David Cébron, Asif Ud-Doula, Evelyne Alecian

► **To cite this version:**

Jérémie Vidal, David Cébron, Asif Ud-Doula, Evelyne Alecian. Fossil field decay due to nonlinear tides in massive binaries. 2019. insu-02049328v1

HAL Id: insu-02049328

<https://insu.hal.science/insu-02049328v1>

Preprint submitted on 26 Feb 2019 (v1), last revised 8 Sep 2019 (v2)

HAL is a multi-disciplinary open access archive for the deposit and dissemination of scientific research documents, whether they are published or not. The documents may come from teaching and research institutions in France or abroad, or from public or private research centers.

L'archive ouverte pluridisciplinaire **HAL**, est destinée au dépôt et à la diffusion de documents scientifiques de niveau recherche, publiés ou non, émanant des établissements d'enseignement et de recherche français ou étrangers, des laboratoires publics ou privés.

Fossil field decay due to nonlinear tides in massive binaries

J. Vidal¹★, D. Cébron², A. ud-Doula³, E. Alecian⁴

¹ *Department of Applied Mathematics, School of Mathematics, University of Leeds, Leeds, LS2 9JT, UK*

² *Université Grenoble Alpes, CNRS, ISTERRE, F-38000 Grenoble*

³ *Penn State Scranton, 120 Ridge View Drive, Dunmore, PA 18512, USA*

⁴ *Université Grenoble Alpes, IPAG, CNRS, F-38000 Grenoble, France*

Accepted XXX. Received YYY; in original form ZZZ

ABSTRACT

Surface magnetic fields have been detected in 5% to 10% of isolated massive stars, hosting outer radiative envelopes. They are often thought to have a fossil origin, i.e. inherited from the stellar formation phase. Yet, magnetic massive stars are scarcer in (close) short-period binaries, as reported by the BinaMiCS collaboration. Thus, different physical conditions in the molecular clouds giving birth to isolated stars and binaries are commonly invoked. Here, we suggest that the observed lower magnetic in binaries is due to nonlinear tides. Close binaries are likely prone to the tidal instability, a fluid instability growing upon the equilibrium tide via nonlinear effects. However, its outcome in radiative interiors is poorly understood. We investigate the tidal instability in rapidly rotating, stably stratified fluids permeated by fossil fields. First, we show that the tidal instability is generated by triadic resonances involving inertia-gravity waves in short-period massive binaries. Second, we build a mixing-length theory of the turbulent mixing generated by nonlinear tides. The predictions are confronted to proof-of-concept simulations. The typical time scale for the turbulent decay of a fossil field evolves as $(\beta_0^2 \Omega_s)^{-1}$, with Ω_s the typical spin angular velocity of the fluid and β_0 the tidal amplitude. Hence, we predict that the tidal disruption of fossil fields would occur in less than a few million years for typical short-period massive binaries (with $\beta_0 \sim 10^{-3} - 10^{-2}$). Therefore, the observed dearth of short-period magnetic binaries may be explained by the mixing generated by nonlinear tides.

Key words: waves – instabilities – binaries: close – stars: magnetic field – stars: massive

1 INTRODUCTION

1.1 Massive stars and magnetic incidence

The magnetism of massive stars has sparked the interest of astronomers for a long time (Babcock 1958). More recently, large spectropolarimetric surveys of these stars have been carried out, such as MiMeS (Wade et al. 2015; Grunhut et al. 2016) or BOB (Hubrig et al. 2014). They have detected surface magnetic fields in 5 to 10% of pre-main sequence and main-sequence massive stars (e.g. Alecian et al. 2017; Mathys 2017). In addition, a magnetic dichotomy has been evidenced between the strong magnetism of chemically peculiar A/B stars (e.g. Auriere et al. 2007; Sikora et al. 2018) and the ultra-weak magnetism of Vega-like stars (Lignieres et al. 2009; Petit et al. 2010, 2011; Blazère et al. 2016). The origin of these fields is unclear. According to stellar evolution theory, massive stars host thick outer radiative

envelopes, which are stably stratified in density. These envelopes are often supposed to be motionless in standard stellar models (e.g. Kippenhahn et al. 1990). This severely challenges the classical dynamo mechanism (Parker 1979), which requires internal turbulent motions (e.g. convection in low-mass stars). Some dynamo mechanisms have been proposed, e.g. relying on the convection of the innermost convective core (Brun et al. 2005; Featherstone et al. 2009) generating magnetic flux tubes rising the stellar surface (MacGregor & Cassinelli 2003; MacDonald & Mullan 2004), on differentially rotating flows (Spruit 1999, 2002; Braithwaite 2006; Jouve et al. 2015) or on baroclinic flows (Simitev & Busse 2017). However, the relevance of these mechanisms remains elusive and debated.

The most accepted assumption is that the fields in massive stars have a fossil origin (Borra et al. 1982; Moss 2001), since they appear relatively stable over the observational period. The fields would be shaped in the stellar formation phase and would survive into later stages of stellar evolution. The fossil theory is now well supported by the existence of

★ j.n.vidal@leeds.ac.uk

magnetic configurations stable enough to survive in stars over their lifetimes (Braithwaite & Spruit 2004; Braithwaite & Nordlund 2006; Reisenegger 2009; Duez & Mathis 2010; Duez et al. 2010; Akgün et al. 2013). Hence, the fossil theory may provide a unifying explanation for the magnetism of intermediate-mass stars (Braithwaite & Spruit 2017). However, the fossil hypothesis still suffers from several weaknesses. In particular, we may naively expect all massive stars to exhibit surface magnetic fields. This is not consistent with the observations (e.g. Alecian et al. 2017; Mathys 2017). Moreover, the theory does not explain convincingly the observed magnetic bi-modality (e.g. Auriere et al. 2007). To solve these issues, different physical conditions in the star-forming regions are usually invoked (e.g. Commerçon et al. 2010, 2011; Braithwaite & Cantiello 2012).

An efficient way to assess this hypothesis is to survey close binaries. Although the formation of binaries is not well understood, we can reasonably assume that the two binary components have been formed together, under similar physical conditions. Then, observing magnetic fields in the two components of a binary system would provide constraints to disentangle initial condition effects from other possible physical effects. The BinaMIcS collaboration (Alecian et al. 2014a) surveyed short-period massive binaries, aiming at providing new constraints on the magnetic properties of massive stars. About 170 short-period double-lined spectroscopic binary (SB2) binary systems on the main-sequence have been analysed (Alecian & et al. 2019). They have typical orbital periods $T_{\text{orb}} \leq 20$ days and a separation distance between the two components $D \leq 1$ au.

A magnetic incidence of about 1.5 % has been measured in the BinaMIcS sample (Alecian et al. 2017). This is much lower to what is typically found in isolated hot stars (see above). Therefore, it appears that radiative stars in short-period binary systems are much less frequently magnetic than in isolated systems. This confirms the general trend observed in other studies, dedicated to intermediate-mass A-type stars (e.g. Carrier et al. 2002; Mathys 2017), and extend it to hotter and more massive stars. Note also that magnetic fields have been mostly observed only in one of the two components of the close binaries (Alecian et al. 2017), with a notable exception in ϵ Lupi system (Shultz et al. 2015). If initial conditions were solely responsible for the presence or not of a fossil field, then we would naively expect that the two components of a magnetic binary should host fossil fields. This is clearly not a general trend. Thus, these puzzling observations defy the theories which are commonly invoked. Notably, is it due to formation processes (Commerçon et al. 2011; Schneider et al. 2016), that exclude more magnetic fields in binaries than in single stars? Or is there any other mechanism in close binaries, responsible for relatively quick dissipation of magnetic fields?

1.2 Mixing in radiative (stratified) interiors

An alternative scenario is to invoke some kind of mixing in the radiative envelopes, that may destroy the pervading fossil fields dynamically. Identifying mixing sources in radiative stars is a long standing issue (see the review of Zahn 2008), since mixing also affects the transports of chemical elements and of angular momentum. Shear-driven turbulence, induced by the (expected) differential rotation of ra-

diative envelopes (e.g. Goldreich & Schubert 1967; Rieutord 2006; Hypolite et al. 2018), has been largely investigated (e.g. Zahn 1974; Mathis et al. 2004, 2018).

A more efficient mixing in short-period stellar binaries may be provided by tides. Indeed, short-periods binaries are strongly deformed (e.g. Chandrasekhar 1969; Lai et al. 1993). Tides proceed in two steps. First, they generate a quasi-hydrostatic tidal bulge, known as the equilibrium tide velocity field (Zahn 1966; Remus et al. 2012), leading to angular momentum exchange between the orbital and spinning motions. Second, they induce dynamical tides (e.g. Zahn 1975; Rieutord & Valdetaro 2010), i.e. waves that propagate within the radiative regions. Radiative envelopes support the propagation of many waves, which are continuously emitted by several mechanisms (e.g. Gastine & Dintrans 2008a,b; Mathis et al. 2014). Among them, internal gravity waves (Dintrans et al. 1999; Mirouh et al. 2016) do induce mixing processes in radiative regions (Schatzman 1993; Rogers & McElwaine 2017).

However, the aforementioned tidal effects are only linear processes. They are likely relevant for weak tides in the solar and extra-solar planets (Ogilvie 2009), but they may be inefficient to disrupt fossil fields on their own. Moreover, nonlinear effects can significantly modify the outcome of the tidal response. Indeed, the equilibrium tide flow can be unstable against the tidal instability (e.g. Rieutord 2004; Le Bars et al. 2010; Vidal & Cébron 2017). The latter instability is a fluid instability, associated with nonlinear triadic resonances between two waves and the equilibrium tide velocity field (Kerswell 2002). The nonlinear saturation of the tidal instability can exhibit a wide variety of nonlinear states in homogeneous fluids such as space-filling small-scale turbulence (Le Reun et al. 2017, 2018) or even global mixing (Grannan et al. 2016; Vidal et al. 2018).

Yet, the fate of the tidal instability in stratified fluid interiors is poorly known. On the one hand, theoretical studies have shown that an axial density stratification, i.e. aligned with the spin angular velocity, has stabilising effects (Miyazaki & Fukumoto 1991, 1992). Moreover, in the equatorial regions, a radial stratification can either increase or decrease the growth rate of the instability (Kerswell 1993a; Le Bars & Le Dizès 2006; Cébron et al. 2013). On the other hand, three-dimensional numerical simulations suggest that the tidal instability is largely unaffected in stratified interiors, for a wide range of stratification (Cébron et al. 2010; Vidal et al. 2018). Therefore, a consistent global picture of the tidal instability in stably stratified interiors is highly desirable. Indeed, this is a prerequisite to assess the astrophysical relevance of the tidal instability for the stellar mixing in close massive binaries.

1.3 Motivations

The present study has a twofold purpose. First, we aim to propose a predictive global theory of the tidal instability in idealised stratified interiors. Such a theory should accurately predict the onset of the instability, reconciling previous theoretical analyses (Miyazaki & Fukumoto 1992; Miyazaki 1993; Kerswell 1993a; Le Bars & Le Dizès 2006) and numerical studies (Cébron et al. 2010; Vidal et al. 2018) within a single framework. Then, asymptotic predictions for the (nonlinear) tidal mixing, as found numerically in (Vidal et al. 2018),

must be obtained to carry out the astrophysical extrapolation. Second, we aim to propose a new physical scenario of tidal disruption of fossil fields, compatible with the observed lower magnetic incidence in short-period massive binaries as analysed by the BinaMIcS collaboration (Alecian et al. 2017; Alecian & et al. 2019).

The paper is organised as follows. In §2, we present the idealised model. In §3, we investigate the linear of the tidal instability in stratified interiors. Then, we develop an heuristic, mixing-length theory of the tidal mixing in §4, which is confronted against proof-of-concept simulations. Hence, we propose a novel scenario for close binaries in §5, which is then applied to short-period double-lined spectroscopic binary (SB2) systems. Finally, we end the paper with a conclusion in §6 and outline some perspectives.

2 FORMULATION OF THE PROBLEM

2.1 Assumptions

The full astrophysical problem is rather complex. Hence, we consider an idealised model, for which numerical simulations can be conducted and confronted against theory. We describe here the main assumptions, as they will be used throughout the paper. Our model retains the essential features that govern the tidal instability, i.e. rotation, stratification, magnetic fields and a tidally deformed geometry.

We consider a primary self-gravitating body, filled with an electrically conducting and rotating fluid of mass M_1 and volume \mathcal{V} . Radiative fluid envelopes are expected to undergo differential rotation (Goldreich & Schubert 1967), e.g. provided by the contraction occurring during the pre-main-sequence phase or baroclinic torques (Busse 1981, 1982; Rieutord 2006). However, differential rotation tends to be smoothed out by hydromagnetic effects. In particular, differential rotation may sustain the magneto-rotational instability, ultimately leading a state of solid-body rotation (Arlt et al. 2003; Rüdiger et al. 2013, 2015) on a few Alfvén timescale (Jouve et al. 2015). Consequently, we assume that the radiative envelope is uniformly rotating.

Then, the primary is orbited by a companion star of mass M_2 . We investigate here only short-period, non-coalescing binaries. Due to the combined action of rotation and of the gravitational potential, the shape of each binary component depart from the spherical geometry. We do not seek here the mutual tidal interactions between the primary and the secondary. Indeed, at the leading order, the primary (or the secondary) is a triaxial ellipsoid in solid-body rotation (e.g. Chandrasekhar 1969; Lai et al. 1993), as obtained by modelling the other component by a point-mass companion. Therefore, for the sake of simplicity, we treat the secondary as a point mass for the orbital dynamics (e.g. Hut 1981, 1982).

The secondary rises an equilibrium tide (Zahn 1966; Remus et al. 2012) on the fluid primary, with a typical equatorial amplitude denoted β_0 . An initially eccentric binary system, with non-synchronised rotating components, evolves towards an orbital configuration characterised by a circular orbit and, ultimately, the system will be synchronised (Hut 1981, 1982). For weakly elliptic orbits, Nduka (1971) showed that the ellipsoidal distortion β_0 points toward the

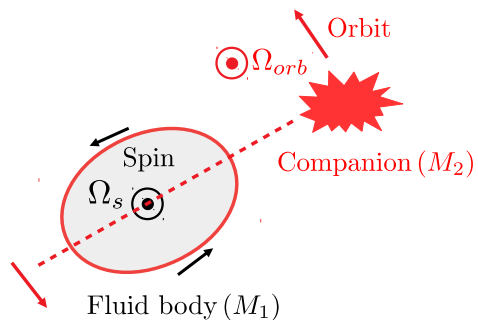


Figure 1. Sketch of the idealised orbital configuration (coplanar and aligned spin and orbit angular velocities), seen from above in the inertial frame.

tidal companion at the leading order. Vidal & Cébron (2017) also showed that weak orbital eccentricities have little effects on the internal fluid dynamics of the primary at the leading order in the eccentricity. Thus, we assume that the binary system is circularised (or weakly eccentric), with an equatorial bulge aligned with the orbital companion.

Then, we consider only the leading-order component of the tidal potential, associated with the asynchronous tides (Ogilvie 2014). Thus, the fluid spin and orbital angular velocities are coplanar and aligned in the inertial frame. Note that this is the expected equilibrium state of the system (e.g. Chandrasekhar 1969). The other tidal components, e.g. obliquity tides, are mainly responsible for additional fluid instabilities which are superimposed on the tidal instability (e.g. Kerswell 1993b). They can be neglected for a first attempt.

Within the fluid primary, diffusive effects are of second order for the tidal instability, in the absence of significant surface diffusive effects at a free boundary (Rieutord 1992; Rieutord & Zahn 1997). Hence, we assume that the fluid has a uniform kinematic viscosity ν , a radiative (thermal) diffusivity κ_T (Kippenhahn et al. 1990) and a magnetic diffusivity $\eta = 1/(\mu_0\sigma)$, where σ is the electrical conductivity and μ_0 the magnetic permeability of free space. Finally, Clausen & Tilgner (2014) showed that the fluid compressibility has almost no effect on the tidal instability. Therefore, we model density variations departing from the isentropic profile within the Boussinesq approximation (Spiegel & Veronis 1960).

2.2 Governing equations

The radiative star is modelled as a tidally deformed, uniformly rotating and stably stratified fluid domain in the Boussinesq approximation. The fluid domain, of typical density $\rho_M = M_1/\mathcal{V}$, is rotating at the angular velocity Ω_s in the inertial frame. The orbital configuration is illustrated in figure 1. The orbital angular velocity in the inertial frame is denoted $\Omega_{orb} \mathbf{1}_z$, with $\Omega_{orb} \neq \Omega_s$ for a non-synchronised orbit. an ellipsoid in the central frame (e.g. Chandrasekhar 1969; Lai et al. 1993). In the central frame, in which the shape is stationary, the outer boundary $\partial\mathcal{V}$ of the fluid domain describes an ellipsoid (e.g. Chandrasekhar 1969; Lai et al. 1993). Its mathematical expression in Cartesian coordinates

NUMBER	SYMBOL	CZ	RZ
Ekman	Ek	10^{-16}	10^{-18}
Prandtl	Pr	10^{-6}	10^{-6}
Magnetic Prandtl	Pm	10^{-6}	10^{-6}
Magnetic Ekman	Em	10^{-12}	10^{-10}
Brunt-Väisälä	N_0/Ω_s	0	0 – 100
Lehnert	Le	10^{-5}	$\leq 10^{-5}$

Table 1. Typical values of the dimensionless numbers. CZ: stellar convective zones, e.g. in the Sun (Charbonneau 2014). Note that $N_0 = 0$ in convective envelopes. RZ: (rapidly) rotating radiative zones (e.g. Rieutord 2006). The order of magnitude of the Lehnert number in RZ has been estimated from the typical values for the scarce short-period magnetic binaries given in table 4.

ordinates (x, y, z) is

$$\left(\frac{x}{a}\right)^2 + \left(\frac{y}{b}\right)^2 + \left(\frac{z}{c}\right)^2 = 1, \quad (1)$$

where (a, b, c) are the semi-axes. The equatorial ellipticity is defined by $\beta_0 = |a^2 - b^2|/(a^2 + b^2)$.

In the following, we work in dimensionless variables. They are written without *, to distinguish them from their dimensional counterparts. To do so, we choose a typical radius R of the fluid domain as unit of length, Ω_s^{-1} as a unit of time, $\Omega_s^2 R/(\alpha_T g_0)$ as unit of the temperature with g_0 a typical value of the gravity field at the outer boundary and α_T the thermal expansion coefficient (at constant pressure). For the magnetic field, we choose $\Omega_s R/\sqrt{\rho_M \mu_0}$ as typical unit. We also introduce the dimensionless orbital frequency $\Omega_0 = \Omega_{\text{orb}}/\Omega_s$. The dimensionless nonlinear equations in the rotating central frame governing the dimensionless velocity field $\mathbf{v}(\mathbf{r}, t)$, temperature $T(\mathbf{r}, t)$ and magnetic field $\mathbf{B}(\mathbf{r}, t)$ at the position \mathbf{r} and time t are momentum, energy and induction equations. They read

$$\frac{\partial \mathbf{v}}{\partial t} = -(\mathbf{v} \cdot \nabla) \mathbf{v} - 2\Omega_0 \mathbf{1}_z \times \mathbf{v} - \nabla(P + P_m) + Ek \nabla^2 \mathbf{v} - T\mathbf{g} + (\mathbf{B} \cdot \nabla) \mathbf{B}, \quad (2a)$$

$$\frac{\partial T}{\partial t} = -(\mathbf{v} \cdot \nabla) T + \frac{Ek}{Pr} \nabla^2 T + Q, \quad (2b)$$

$$\frac{\partial \mathbf{B}}{\partial t} = \nabla \times (\mathbf{v} \times \mathbf{B}) + Em \nabla^2 \mathbf{B}, \quad (2c)$$

$$\nabla \cdot \mathbf{v} = \nabla \cdot \mathbf{B} = 0, \quad (2d)$$

with P the hydrostatic pressure (including centrifugal effects), $P_m = |\mathbf{B}|^2/2$ the magnetic pressure, Q a heat source term and $\mathbf{g} = -\nabla\Phi_0$ the (imposed) gravity field in the Boussinesq approximation. In governing equations (2), we have introduced as dimensionless numbers the Ekman number $Ek = \nu/(\Omega_s R^2)$, the Prandtl number $Pr = \nu/\kappa_T$, the magnetic Prandtl number $Pm = \nu/\eta$ and the magnetic Ekman number $Em = Ek/Pm$. Typical values are given in table 1 for stellar interiors. The latter are characterised by weakly diffusive conditions (i.e. $Ek, Ek/Pr, Ek/Pm \ll 1$). This regime will greatly simplify the analysis of the tidal instability.

We do not solve directly the full equations (2). Indeed, a reference ellipsoidal state is always first established, on which the tidal instability grows upon and saturates nonlinearly. We expand the field variables as perturbations (not

necessarily small) around a steady reference ellipsoidal basic state $[\mathbf{U}_0, T_0, \mathbf{B}_0]$ (detailed later). Thus, the dimensionless nonlinear governing equations for the perturbations $[\mathbf{u}, \Theta, \mathbf{b}](\mathbf{r}, t)$ are

$$\frac{d\mathbf{u}}{dt} + (\mathbf{u} \cdot \nabla) \mathbf{u} = -\mathbf{u} \cdot \nabla \mathbf{U}_0 - 2\Omega_0 \mathbf{1}_z \times \mathbf{u} - \nabla(p + p_m) + Ek \nabla^2 \mathbf{u} - \Theta \mathbf{g} + (\mathbf{B}_0 \cdot \nabla) \mathbf{b} + (\mathbf{b} \cdot \nabla) \mathbf{B}_0, \quad (3a)$$

$$\frac{d\Theta}{dt} + (\mathbf{u} \cdot \nabla) \Theta = -(\mathbf{u} \cdot \nabla) T_0 + \frac{Ek}{Pr} \nabla^2 \Theta, \quad (3b)$$

$$\frac{\partial \mathbf{b}}{\partial t} + \nabla \times (\mathbf{b} \times \mathbf{u}) = \nabla \times (\mathbf{U}_0 \times \mathbf{b} + \mathbf{u} \times \mathbf{B}_0) + Em \nabla^2 \mathbf{b}, \quad (3c)$$

$$\nabla \cdot \mathbf{u} = \nabla \cdot \mathbf{b} = 0, \quad (3d)$$

with $d/dt = \partial/\partial t + (\mathbf{U}_0 \cdot \nabla)$ the material derivative along the basic flow (7), p the hydrodynamic pressure, and the magnetic pressure $p_m = \mathbf{B}_0 \cdot \mathbf{b}$. For the proof-of-concept simulations in §4, the equations will be supplemented by appropriate boundary conditions.

2.3 Reference ellipsoidal configuration

We consider a steady reference equilibrium state, for which isopycnals coincide with isopotentials for Φ_0 (including centrifugal force, self-gravity and tides). This assumption is consistent with compressible models (Lai et al. 1993). Hence, we assume that the background temperature profile $T_0(\mathbf{r})$ and the gravity field \mathbf{g} , solutions of equations (2a)-(2b) are in a barotropic state (for a well-chosen Q), i.e. $\mathbf{g} \times \nabla T_0 = \mathbf{0}$. We neglect the baroclinic part, which is known to enhance the growth rate of the tidal instability in the equatorial plane (Kerswell 1993a; Le Bars & Le Dizès 2006). In the nonlinear regime, a baroclinic state would certainly also enhance the tidal turbulence in stellar interiors. However, we focus here on the less favourable configuration for growth of the tidal instability (i.e. barotropic stratification). This choice is also consistent with the assumed uniform rotation of the fluid. Indeed, baroclinic torques are known to sustain differential rotation (e.g. Busse 1981, 1982; Rieutord 2006). Moreover, considering a barotropic state is a relevant assumption when the isopycnals move sufficiently fast to keep track of the rotating tidal potential (Ogilvie 2014). This situation is expected when the stratification has a large enough amplitude compared to the differential rotation $\Omega_s - \Omega_{\text{orb}}$ between the spin and the orbit.

To characterise the stratification, we introduce the dimensional (local) Brunt-Väisälä frequency N in the reference state. In dimensional variables, the latter is defined by

$$N^2 = -\alpha_T \mathbf{g}^* \cdot \nabla T_0^*. \quad (4)$$

The fluid ellipsoid is assumed to be entirely stably stratified in density, i.e. $N^2 > 0$. The exact profiles in stellar interiors depend on the stellar internal processes. However, we aim at comparing analytical and numerical computations, which cannot be done for arbitrary profiles. Thus, we assume that the dimensionless total gravitational potential is quadratic, i.e.

$$\Phi_0 = \frac{x^2}{a} + \frac{y^2}{b} + \frac{z^2}{c}. \quad (5)$$

Then, we consider the (dimensionless) reference temperature in barotropic equilibrium $T_0 = (N_0^2/\Omega_s^2) \Phi_0$, with N_0 a typical value of the Brunt-Väisälä frequency at the outer boundary.

For intermediate-mass stars with $M_1 = 3M_\odot$ (where M_\odot is the solar mass), a typical value is $N_0 \sim 10^{-3} \text{ s}^{-1}$ (e.g. Rieutord 2006), and typical values of Ω_s^{-1} range between 1 and 100 days (Mathys 2017). This yields $0 \leq N_0/\Omega_s \leq 100$ in radiative stars. Hence, a barotropic reference configuration is a reasonable starting assumption.

Then, the ellipsoid is permeated by an imposed fossil magnetic field $\mathbf{B}_0(\mathbf{r})$ (in dimensionless form). To measure the relative strength of magnetic and rotational effects, we introduce the (dimensionless) Lehnert number (Lehnert 1954)

$$Le = \frac{B_0^*}{\Omega_s R \sqrt{\rho_M \mu_0}}. \quad (6)$$

where B_0^* is the typical (dimensional) strength of the fossil field. The Lehnert number is the ratio of the Alfvén and rotational velocities. When $Le \ll 1$, the Coriolis force dominates over the Lorentz force in momentum equation (2a). The regime $Le \ll 1$ is encountered in many magnetic stars (table 1). In the Sun, a typical value is $Le \sim 10^{-5}$ (Charbonneau 2014). For the scarce magnetic binaries which have been observed, the median field strength is $B_0^* \sim 1 \text{ kG}$ (see also values in table 4). This yields as typical values $Le \leq 10^{-5} - 10^{-4}$. Hence, we focus on the regime $Le \ll 1$ in the following.

Finally, the orbital configuration drives the equilibrium tidal flow (e.g. Remus et al. 2012). For non-synchronised orbits ($\Omega_0 \neq 1$), its leading-order flow components in the central frame are (e.g. Cébron et al. 2012b; Vidal & Cébron 2017)

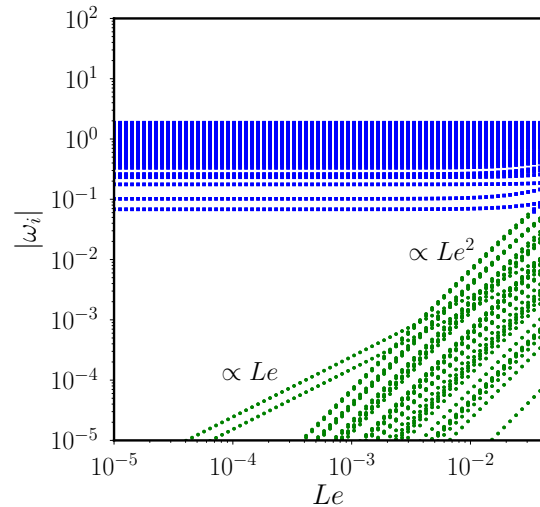
$$\mathbf{U}_0(\mathbf{r}) = (1 - \Omega_0) [-(1 + \beta_0)y \mathbf{1}_x + (1 - \beta_0)x \mathbf{1}_y]. \quad (7)$$

This is an exact incompressible solution of the nonlinear hydrodynamic momentum equation (2a). Moreover, it satisfies the no-penetration $\mathbf{U}_0 \cdot \mathbf{1}_n = 0$ at the boundary $\partial\mathcal{V}$, with $\mathbf{1}_n$ the unit outward normal vector. Note that the basic flow (7) is not rigorously a solution in the presence of an arbitrary magnetic field. Yet, the large-scale poloidal and toroidal components of $\mathbf{B}_0(\mathbf{r})$ are unlikely to modify the equilibrium tide flow (Kerswell 1993a, 1994; Mizerski & Bajer 2011).

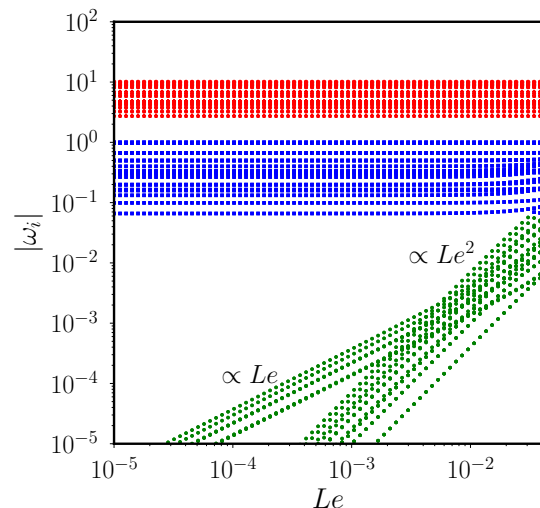
2.4 Hydromagnetic waves

In the absence of any driving mechanism, a fossil field \mathbf{B}_0 slowly decays on the Ohmic diffusive timescale $(\Omega_s Ek/Pm)^{-1}$. This time is larger than the typical lifetime of least massive stars on the main-sequence (e.g. Braithwaite & Spruit 2017). However, equations (3) support the propagation of several waves, which can strongly modify the dynamical evolution of radiative envelopes. In the presence of tides, it turns out that the waves can be nonlinearly coupled with the equilibrium tide velocity field \mathbf{U}_0 , yielding the tidal instability (e.g. Kerswell 1993a; Vidal & Cébron 2017). This clearly shows that the wave dynamics is a key phenomenon in radiative stars. Hence, identifying the different families in our system is a prerequisite.

The wave properties have already been outlined in unbounded geometries (e.g. Gubbins & Roberts 1987; Mathis & de Brye 2011; Sreenivasan & Narasimhan 2017). These unbounded waves have global bounded counterparts, known as Magneto-Archimedean-Coriolis (MAC) modes. In appendix A, we present a new algorithm to compute the MAC modes



(a) Neutral fluid ($N_0/\Omega_s = 0$)



(b) Stratified fluid ($N_0/\Omega_s = 10$)

Figure 2. Spectrum $|\omega_i|$ as a function of Le for large-scale MAC modes in the unperturbed geometry ($\beta_0 = 0$), stratified under the gravitational potential (5). The background (toroidal) magnetic field is $\mathbf{B}_0 = 0.1 [-z \mathbf{1}_y + y \mathbf{1}_z] + [-y \mathbf{1}_x + x \mathbf{1}_y]$ in dimensionless form. From bottom to top: green circles are slow MC and torsional modes (respectively scaling in Le and Le^2), blue squares fast MC modes and red stars gravito-inertial modes. The truncation polynomial degree is $n = 5$, see appendix A for details.

in arbitrary triaxial ellipsoids (e.g. tidally deformed bodies). The dimensionless eigenfrequency ω_i of MAC modes in full ellipsoids is shown in figure 2, for the relevant regime $Le \leq 10^{-1}$. We have considered an arbitrary reference configuration to illustrate several representative properties of the modes.

We identify three families of waves in neutrally stratified fluids (figure 2a), in agreement with investigations in

spherical geometries (e.g. Schmitt 2010; Labbé et al. 2015). First, the high frequency branch represents fast Magneto-Coriolis (MC) modes (Malkus 1967; Labbé et al. 2015). They are similar to pure Coriolis modes (Greenspan 1968; Vantieghem 2014; Backus & Rieutord 2017), with the spectrum $|\omega_i| \leq 2$ in the regime $Le \ll 1$. These modes are regular in space and only weakly affected by large-scale magnetic fields in weakly deformed spheres (e.g. Schmitt 2010; Labbé et al. 2015), as observed by the frequency dependence on Le in the figure. Note that their behaviour is different than the singular modes, localised on attractors (e.g. Rieutord & Valdettaro 1997, 2018), that only exist in shells because the mathematical problem is ill-posed (Rieutord et al. 2000). Second, the low frequency branch represents slow Magneto-Coriolis modes. Their typical dimensionless frequency scales as $|\omega_i| \propto Le^2$. Braithwaite & Cantiello (2012) proposed that these Magneto-Coriolis modes are responsible for the expected failed-fossil origin of the ultra weak magnetic fields in Vega-like stars. Indeed, these fields may be the remnants of some fields inherited after star formation phase and may evolve dynamically on the timescale $Le^{-2} \Omega_s^{-1}$, which can be roughly equal to the age of intermediate-mass stars. In addition, the third intermediate branch represents torsional Alfvén modes (Labbé et al. 2015), scaling as $|\omega_i| \propto Le$. They are usually filtered out in reduced models, e.g. in local models considering uniform fields. They exist when the current direction $\nabla \times \mathbf{B}_0$ of the basic state is misaligned with the spin rotation axis Ω_s .

Then, we show the spectrum of MAC modes in stratified fluids in figure 2b. The aforementioned hydromagnetic modes still exist in stably stratified interiors, yielding fast and slow MAC waves. However, their properties in the presence of buoyancy and magnetic fields are rather complex in spherical-like domains (Friedlander 1987). On the one hand, fast MAC modes and gravito-inertial modes are barely modified by magnetic fields, as illustrated in figure 2b when $Le \ll 1$. However, they strongly depend on the stratification (Friedlander & Siegmund 1982a). On the other hand, slow MC modes can be strongly affected by the magnetic field and the stratification (Friedlander 1987). Finally, the buoyancy force also sustains high frequency internal gravity modes. They can be affected by the rotation, yielding gravito-inertial modes (Friedlander & Siegmund 1982a).

3 ONSET OF THE TIDAL INSTABILITY

In this section, we present the stability analysis of the tidal instability at the onset. First, we outline the general stability method in §3.1. In §3.2, we present some analytical computations valid in the equatorial and polar regions, to get a physical insight of the instability mechanism. Then, we solve the stability equations in the whole stellar interior in §3.3 and §3.4. Finally, we discuss the magnetic effects in §3.5.

3.1 Stability theory

3.1.1 Triadic couplings

It has been recognised for a long time that the tidal instability is a parametric instability (Malkus 1989). It is due to

triadic interactions between pairs of modes that are coupled with the underlying flow (7). A fluid instability can grow upon the reference configuration provided that resonance conditions are met in time and space (Le Dizès 2000). A necessary condition for instability is given by the time resonance condition in the central frame (Kerswell 2002; Vidal & Cébron 2017)

$$|\omega_i - \omega_j + \delta| = 2|1 - \Omega_0|, \quad (8)$$

where $[\omega_i, \omega_j]$ are the angular frequencies of two free waves and δ a small detuning parameter ($\delta \rightarrow 0$ for diffusionless fluids) allowing for imperfect resonances (Lacaze et al. 2004; Cébron et al. 2012a, 2014), due to either diffusive (e.g. Kerswell 1993a) or topographic effects (e.g. Le Dizès 2000). Detuning effects are negligible in the astrophysical regime (almost diffusionless and with $\beta_0 \ll 1$). Note that the case of synchronised orbits $\Omega_0 = 1$ (in average) is forbidden by condition (8). Thus, synchronised orbits must be treated separately, see appendix B.

We are now in a position to survey the possible non-linear couplings of the different types of modes which yields to tidal instabilities. The MAC modes presented in §2 can be combined in several ways to fulfil condition (8) in non-synchronised systems. From condition (8), the tidal instability traditionally exists in the orbital range $-1 \leq \Omega \leq 3$ (e.g. Vidal & Cébron 2017). The associated triadic interactions necessarily involve fast MAC waves coupled with either fast or a slow MAC waves (Kerswell 1993a, 1994). Indeed, in the astrophysical regime $Le \ll 1$, the spectrum illustrated in figure 2 clearly shows that no triadic couplings are effective in ellipsoids between two slow MAC waves. Thus, the couplings of slow MAC waves with the equilibrium tide flow cannot be advocated in stellar interiors.

Among the aforementioned resonances, sub-harmonic resonances are characterised by $\omega_i = -\omega_j$. Then, the resonance condition (8) reduces (in the diffusionless regime) to

$$|\omega_i| = |1 - \Omega_0|. \quad (9)$$

which is a necessary stability condition for a sub-harmonic instability. Sub-harmonic resonances have been found to be the most unstable in homogeneous fluids (Kerswell 1993a, 1994; Le Dizès 2000; Vidal & Cébron 2017), i.e. yielding the largest growth rates σ . For the tidal instability, only fast MAC waves can fulfil the sub-harmonic resonance condition (9). To clarify the underlying structure at the resonance of fast MAC waves, we first treat the non-magnetic case (i.e. $Le = 0$). Indeed, the addition of the magnetic field has only second-order effects (see §3.5).

3.1.2 Short-wavelength perturbations

We seek three-dimensional perturbations, solution of the linearised equations (3) and satisfying the resonance conditions (8) or (9). Diffusive effects are extremely small in radiative stellar interiors (see table 1). In a first attempt, we can investigate the stability of the reference ellipsoidal configuration by seeking diffusionless perturbations.

The global stability analysis is beyond the scope of the present study. However, in the diffusionless regime, three-dimensional global perturbations of small enough length scales are excited, such that they are not affected by the

boundary. Hence, we consider short-wavelength (WKB) perturbations (Lifschitz & Hameiri 1991; Friedlander & Vishik 1991). They are local perturbations, barely sensitive to the ellipsoidal boundary $\partial\mathcal{V}$, advected along the fluid trajectories $\mathbf{X}(t)$ of \mathbf{U}_0 . The local stability theory is of practical interest, because the stability equations then reduce to ordinary differential equations in the Lagrangian description. The local stability behaviour should be obtained in the global stability analysis by a limiting process, as argued by Lifschitz (1995). This has been confirmed in homogeneous cylinders (Kerswell 1993a) and ellipsoids (Vidal & Cébron 2017).

In appendix C, we have extended the general local stability theory to account for magnetic effects within the Boussinesq approximation. Here, we consider only the hydrodynamic Boussinesq stability equations, by seeking Eulerian perturbations upon the equilibrium tidal flow in the form

$$[\mathbf{u}, \Theta](\mathbf{r}, t) = [\widehat{\mathbf{u}}, \widehat{\Theta}](\mathbf{r}, t) \exp(i\mathbf{k} \cdot \mathbf{r}), \quad |\mathbf{k}(t)| = |\mathbf{k}_0|, \quad (10)$$

where $\mathbf{k}(t)$ is the local wave vector with the initial value \mathbf{k}_0 . The stability equations are rather solved in Lagrangian variables, yielding the ordinary differential equations (in dimensionless form)

$$\frac{D\mathbf{X}}{Dt} = \mathbf{U}_0(\mathbf{X}), \quad \mathbf{X}(0) = \mathbf{X}_0, \quad (11a)$$

$$\frac{D\mathbf{k}}{Dt} = -(\nabla\mathbf{U}_0)^\top \mathbf{k}, \quad \mathbf{k}(0) = \mathbf{k}_0, \quad (11b)$$

$$\begin{aligned} \frac{D\widehat{\mathbf{u}}}{Dt} = & \left[\left(\frac{2\mathbf{k}\mathbf{k}^T}{|\mathbf{k}|^2} - \mathbf{I} \right) \nabla\mathbf{U}_0 + 2 \left(\frac{\mathbf{k}\mathbf{k}^T}{|\mathbf{k}|^2} - \mathbf{I} \right) \Omega_0 \mathbf{1}_z \times \right] \widehat{\mathbf{u}} \\ & - \widehat{\Theta} \left(\mathbf{I} - \frac{\mathbf{k}\mathbf{k}^T}{|\mathbf{k}|^2} \right) \mathbf{g}, \end{aligned} \quad (11c)$$

$$\frac{D\widehat{\Theta}}{Dt} = -(\widehat{\mathbf{u}} \cdot \nabla)T_0, \quad (11d)$$

with D/Dt the Lagrangian time derivative. The solenoidal condition $\widehat{\mathbf{u}} \cdot \mathbf{k} = 0$, is satisfied as long as it holds at the initial time, i.e. $\widehat{\mathbf{u}}(0) \cdot \mathbf{k}_0 = 0$ in the Lagrangian description. Equations (11) do depend on the fluid trajectories $\mathbf{X}(t)$ because the gravity field \mathbf{g} is spatially varying.

Equations (11) are ordinary differential equations along the Lagrangian trajectories $\mathbf{X}(t)$. They are also independent of the magnitude of \mathbf{k}_0 in the diffusionless limit. Hence, we follow Le Dizès (2000) by restricting the initial wave vector to the unit spherical surface

$$\mathbf{k}_0 = \sin(\theta_0) \cos(\phi_0) \mathbf{1}_x + \sin(\theta_0) \sin(\phi_0) \mathbf{1}_y + \cos(\theta_0) \mathbf{1}_z, \quad (12)$$

where $\phi_0 \in [0, 2\pi]$ is the longitude and $\theta_0 \in [0, \pi]$ is the colatitude between the spin axis $\mathbf{1}_z$ and the wave vector \mathbf{k}_0 . In practice, equations (11) are integrated from a range of wave vectors \mathbf{k}_0 and initial positions \mathbf{X}_0 within the reference ellipsoidal domain. The basic state is unstable with respect to short-wavelength perturbations if

$$\lim_{t \rightarrow \infty} \left(|\widehat{\mathbf{u}}(t, \mathbf{X}_0, \mathbf{k}_0)| + |\widehat{\Theta}(t, \mathbf{X}_0, \mathbf{k}_0)| \right) = \infty. \quad (13)$$

Then, we determine the maximum growth rate σ as the fastest growing solution for all initial conditions, i.e. the largest Lyapunov exponent. This yields a sufficient condition for the instability.

3.2 Two limit configurations

The equilibrium tidal flow (7) admits analytical periodic fluid trajectories $\mathbf{X}(t)$ and wave vectors $\mathbf{k}(t)$, solution of equations (11a)-(11b). Thus, we can carry out an asymptotic analysis to solve equations (11), by expanding all quantities $(\mathbf{X}, \mathbf{k}, \widehat{\mathbf{u}}, \widehat{\Theta})$ in successive powers of β_0 (see details in Le Dizès 2000). We present two simple configurations, which are tractable analytically.

3.2.1 Equatorial plane

First, we focus on the equatorial plane $z_0 = 0$. At the leading asymptotic order $\beta_0 = 0$, \mathbf{U}_0 is a solid-body rotation. Resonance condition (9) yields, in the equatorial plane,

$$\sqrt{4(\widetilde{\Omega}_0 + 1)^2 + \widetilde{N}_0^2 x_0^2} \cos(\theta_0) = \pm 1 \quad (14)$$

with $x_0 \leq 1$ the position of the initial trajectory \mathbf{X}_0 in the equatorial plane, the background rotation $\widetilde{\Omega}_0 = \Omega_0/(1 - \Omega_0)$ and $\widetilde{N}_0 = (N_0/\Omega_s)/|1 - \Omega_0|$. Several configurations are possible, depending on the parameters. On the one hand, the LHS of equation (14) is purely imaginary when $-\widetilde{N}_0^2 x_0^2 > 4(\widetilde{\Omega}_0 + 1)^2$, i.e. when the stratification is unstably stratified (with $N_0^2/\Omega_s^2 \leq 0$). Then, a centrifugal instability grows upon the reference configuration, with a maximum (dimensionless) growth rate (e.g. Le Bars & Le Dizès 2006)

$$\frac{\sigma}{|1 - \Omega_0|} = \sqrt{-\widetilde{N}_0^2 x_0^2 - 4(\widetilde{\Omega}_0 + 1)^2}. \quad (15)$$

On the other hand, the tidal instability is triggered when all terms in equation (14) are real. Hence, no sub-harmonic instability is possible when $\widetilde{N}_0^2 x_0^2 < -3 - 4\widetilde{\Omega}_0(2 + \widetilde{\Omega}_0)$. This defines the forbidden zone of the tidal instability in stably stratified fluids, at a given position x_0 . For neutral fluids ($N_0 = 0$), we recover the classical allowable orbital range of the tidal instability $-1 \leq \Omega_0 \leq 3$. Outside this range, we find that waves can be involved in triadic resonances in stratified fluids. Thus, sub-harmonic tidal instabilities may not be forbidden in stratified fluids when $\Omega_0 \leq -1$ and $\Omega_0 \geq 3$ (range known as the forbidden zone in neutral fluids).

At the next asymptotic order (Le Dizès 2000), the dimensionless growth rate in the equatorial plane is

$$\frac{\sigma}{|1 - \Omega_0|} = \frac{(2\widetilde{\Omega}_0 + 3)^2}{16(1 + \widetilde{\Omega}_0)^2 + 4\widetilde{N}_0^2 x_0^2} \beta_0. \quad (16)$$

Hence, as already discussed in the conclusion of Le Bars & Le Dizès (2006), the growth rate σ is weakened by the stratification when x_0 increases. However, note that their formula for this case slightly differs from equation (16). This led us to confirm the validity of our equation (16) by numerical integration of the local stability equations (see later).

We show in figure 3 the maximum growth rate, computed from formula (16), by considering different orbital configurations Ω_0 . Several points are worthy of comment. First, the tidal instability is excited in the equatorial regime when $-1 \leq \Omega_0 \leq 3$ (in the diffusionless limit), i.e. in the classical orbital range of the tidal instability (Le Dizès 2000). This mechanism occurs for any realistic value of $N_0/\Omega_s \leq 100$ (see table 1). In this orbital range, the maximum growth rate

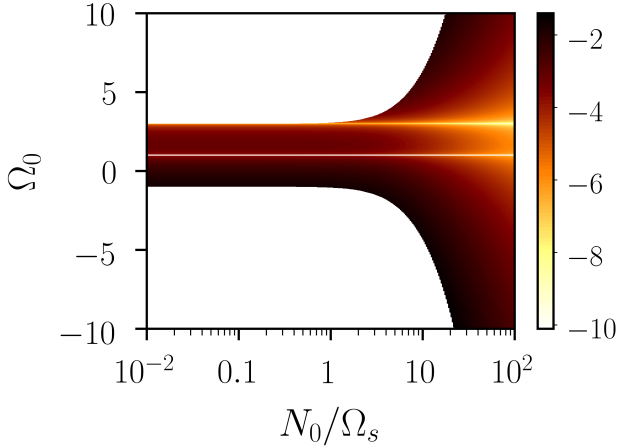


Figure 3. Survey of the growth rate of the tidal instability, predicted by formula (16) in the equatorial plane ($x_0 = 0.5, z_0 = 0$), as a function of $(N_0/\Omega_s, \Omega_0)$. Colour bar shows the normalised ratio $\log_{10}(\sigma/\beta_0)$. White areas correspond to marginally stable areas. For neutral fluids, the tidal instability is restricted to the allowable range $-1 \leq \Omega_0 \leq 3$ when $\beta_0 \ll 1$. When $\Omega_0 = 1$ (horizontal white line), the basic state is synchronised (see appendix B).

is always obtained for neutral fluids ($N_0 = 0$), yielding the usual (dimensionless) growth rate (Le Dizès 2000)

$$\frac{\sigma}{|1 - \Omega_0|} = \frac{(2\widetilde{\Omega}_0 + 3)^2}{16(1 + \widetilde{\Omega}_0)^2} \beta_0. \quad (17)$$

Second, outside the classical orbital range (i.e. in the forbidden zone), we unravel new tidal instabilities, triggered for large enough values of the Brunt-Väisälä frequency (i.e. $N_0/\Omega_s \gg 1$). Their growth rate can be larger than one in our dimensionless units (not shown), because their typical time scale is N_0^{-1} (rather than Ω_s^{-1}). Note that such sub-harmonic resonances have been reported in local stratified simulations (Le Reun et al. 2018).

Therefore, in the equatorial regions, we have shown that a barotropic stratification has (i) a destabilising effect, within the usual forbidden zone (i.e. $\Omega_0 \leq -1$ and $\Omega_0 \geq 3$), and (ii) a stabilising effect when $-1 \leq \Omega_0 \leq 3$. However, we emphasise that a baroclinic state (i.e. $\mathbf{g} \times \nabla T_0 \neq \mathbf{0}$) has the opposite effect (Kerswell 1993a; Le Bars & Le Dizès 2006). This behaviour can be recovered by our asymptotic analysis, by assuming an imposed gravity field with a different equatorial ellipticity $\beta_1 \neq \beta_0$. For such a reference ellipsoidal configuration, formula (16) becomes

$$\frac{\sigma}{|1 - \Omega_0|} = \frac{(2\widetilde{\Omega}_0 + 3)^2}{16(1 + \widetilde{\Omega}_0)^2 + 4\widetilde{N}_0^2 x_0^2} \left| \beta_0 + \widetilde{N}_0^2 x_0^2 \frac{\beta_0 - \beta_1}{2\widetilde{\Omega}_0 + 3} \right|, \quad (18)$$

which corrects misprints in equation (D.1) of Cébron et al. (2012b), obtained with a different unit of time. For circular iso-lines of gravity ($\beta_1 = 0$), formula (16) clearly shows that the growth rate of the tidal instability is enhanced in the equatorial plane. This is the configuration considered by Kerswell (1993a) and Le Bars & Le Dizès (2006). Besides, equation (18) recovers formula (4.7) of Le Bars & Le Dizès (2006) in their particular configuration $\widetilde{\Omega}_0 = 0$.

3.2.2 Polar regions

Now, we focus on the polar regions, by considering initial fluid trajectories close to the spin axis (i.e. $s_0 = \beta_0 \ll 1$). At the leading asymptotic order $\beta_0 = 0$, sub-harmonic resonance condition (9) yields in the central frame

$$\cos^2(\theta_0) = \frac{1 - \widetilde{N}_0^2 z_0^2}{4(\widetilde{\Omega}_0 + 1)^2 - \widetilde{N}_0^2 z_0^2}. \quad (19)$$

The above condition (19) shows that the forbidden zone of the tidal instability coincides with the one for neutral fluid, i.e. $\Omega_0 \leq -1$ and $\Omega_0 \geq 3$. Outside this range, the asymptotic (dimensionless) growth rate is

$$\frac{\sigma}{|1 - \Omega_0|} = \frac{(2\widetilde{\Omega}_0 + 3)^2 (1 - \widetilde{N}_0^2 z_0^2)}{16(1 + \widetilde{\Omega}_0)^2 - 4\widetilde{N}_0^2 z_0^2} \beta_0. \quad (20)$$

Formula (20) is identical to the diffusionless growth rate devised by Miyazaki (1993), denoting $\widetilde{N}_0 z_0$ their local value of the stratification. Hence, an axial stratification is uniformly stabilising along the polar axis.

3.3 Bulk sub-harmonic resonances

The previous analytical analysis shows that a stable stratification ($N_0/\Omega_s \geq 0$) has indubitably a stabilising behaviour in equatorial regions. Moreover, the axial stratification has a stabilising effect, i.e. is responsible for a trapping of the instability in the equatorial region. These observations are in agreement with existing local analyses (Miyazaki & Fukumoto 1992; Miyazaki 1993; Kerswell 1993a; Le Bars & Le Dizès 2006; Cébron et al. 2012b). However, this is barely consistent with three-dimensional numerical simulations (Vidal et al. 2018), showing that the growth rate at the onset is largely unaffected by the stratification. To reconcile these approaches, we investigate the onset of the tidal instability in the whole reference fluid domain. We investigate only non-synchronised orbits, i.e. $\Omega_0 \neq 1$. Synchronised orbits can be studied in a similar fashion, see appendix B.

3.3.1 Families of waves

It turns out that the behaviour of the tidal instability is intrinsically associated with the properties of the waves involved in the sub-harmonic resonances. The wave-like equation in the system, introduced in appendix A, is a mixed hyperbolic-elliptic partial differential equation. In the general case, a wave-like hyperbolic domain coexists with an elliptic domain, in which the waves are evanescent. At the leading asymptotic order $\beta_0 = 0$, Friedlander & Siegmund (1982a) showed that the characteristic curve delimiting the two domains is

$$(4 - \omega_i^2) \left[\omega_i^2 - (N_0/\Omega_s)^2 z^2 \right] = 0. \quad (21)$$

The wave spectrum is divided in two main regimes. On the one hand, we have inertial waves modified by the gravity, called inertial-gravity waves and denoted \mathcal{H} . They have hyperbolic turning surfaces given by equation (21). They are sub-divided in two families

$$\mathcal{H}_1 : (N_0/\Omega_s)^2 < \omega_i^2 < 4, \quad (22a)$$

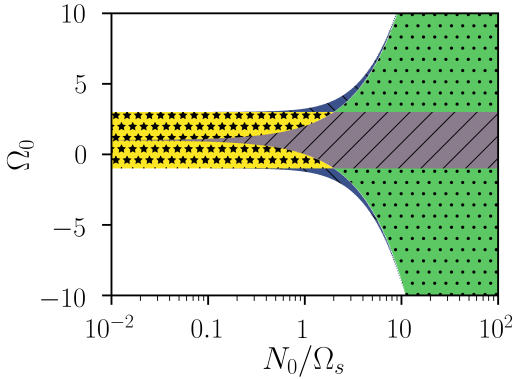


Figure 4. Existence of sub-harmonic resonances as a function of $\Omega_0 = \Omega_{\text{orb}}/\Omega_s$ and N_0/Ω_s . The sub-harmonic resonance condition is given by formula (9) in the central frame. In white regions tidally forced waves do not propagate. Stars (yellow area): hyperbolic waves \mathcal{H}_1 . Right slash (purple area): hyperbolic waves \mathcal{H}_2 . Dots (green area): elliptic waves \mathcal{E}_1 . Back slash (blue area): elliptic waves \mathcal{E}_2 . The classical allowable region of the tidal instability (for neutral fluids) is $-1 \leq \Omega_0 < 3$. wave-like domains ($\mathcal{H}_1, \mathcal{H}_2$) are illustrated in figure 5 (a,b). Similarly, wave-like domains ($\mathcal{E}_1, \mathcal{E}_2$) are illustrated in figure 6 (a,b).

$$\mathcal{H}_2 : 0 < \omega_i^2 < \min[4, (N_0/\Omega_s)^2]. \quad (22b)$$

On the other hand, we have gravity waves modified by the rotation, called gravito-inertial waves and denoted \mathcal{E} . They have ellipsoidal turning surfaces given by equation (21). They are also divided in two families characterised by

$$\mathcal{E}_1 : 4 < \omega_i^2 < (N_0/\Omega_s)^2, \quad (23a)$$

$$\mathcal{E}_2 : \max[4, (N_0/\Omega_s)^2] < \omega_i^2 < 4 + (N_0/\Omega_s)^2. \quad (23b)$$

These properties are quite general, since equation (21) depends solely on the reference state. Therefore, both global modes (e.g. Dintrans et al. 1999) and local waves propagating upon this reference configuration exhibit this distinction.

The different families of waves satisfying the sub-harmonic resonance condition (9) are illustrated in figure 4. This is the main result of the linear theory, as it provides a necessary (and sufficient, see later) condition for the existence of tidal instabilities, in both global modes and local models. Two kinds of tidal instabilities are obtained, depending on the value of key parameter Ω_0 . At the leading asymptotic order, the sub-harmonic resonance condition (9) yields in the local theory

$$\cos^2(\theta_0) = \frac{\bar{\omega} + \bar{N}_0^2 r_0^2 [(\bar{N}_0^2 r_0^2 - \bar{\omega}) \cos^2 \alpha_0 - \cos(2\alpha_0)]}{\bar{\omega}^2 + \bar{N}_0^2 r_0^2 [\bar{N}_0^2 r_0^2 - 2\bar{\omega} \cos(2\alpha_0)]} + \frac{2\sqrt{\omega_1 [\bar{\omega}(1 - \bar{N}_0^2 z_0^2) + \bar{N}_0^2 r_0^2 - 1]}}{\bar{\omega}^2 + \bar{N}_0^2 r_0^2 [\bar{N}_0^2 r_0^2 - 2\bar{\omega} \cos(2\alpha_0)]}, \quad (24)$$

with $\bar{\omega} = 4(1 + \bar{\Omega}_0)^2$, the initial position $\mathbf{X}_0 = (x_0, z_0)^\top = r_0(\sin \alpha_0, \cos \alpha_0)^\top$ where r_0 is the initial radius and $\omega_1 = \bar{N}_0^4 r_0^4 \cos^2 \alpha_0 \sin^2 \alpha_0$. The associated wave-like domains and colatitude angles θ_0 are shown in figures 5 and 6.

3.3.2 Classical orbital range ($-1 \leq \Omega_0 \leq 3$)

The classical allowable range of the instability in homogeneous fluids is $-1 \leq \Omega_0 \leq 3$ (Craig 1989; Le Dizès 2000). Within this range, the sub-harmonic condition involves only \mathcal{H} waves, as shown in figure 4. For a neutral stratification ($N_0 = 0$), they are inertial waves \mathcal{H}_1 , which propagate in the whole fluid cavity (Friedlander & Siegmann 1982a). They have the colatitude angle at the sub-harmonic resonance (Le Dizès 2000)

$$\cos(\theta_0) = \frac{1}{2(1 + \bar{\Omega}_0)} = \frac{1 - \bar{\Omega}_0}{2}. \quad (25)$$

This remains valid in weakly stratified fluids (i.e. $N_0/\Omega_s \ll 1$). Indeed, \mathcal{H}_1 waves are only slightly modified by the buoyancy. They still propagate in the whole fluid domain, as shown in figure 5a. In addition, their colatitude angle θ_0 is slightly increased with respect to formula (25) in the polar regions.

When $N_0/\Omega_s \geq 1$, \mathcal{H}_1 waves morph into \mathcal{H}_2 waves, i.e. inertia-gravity waves. These waves are strongly modified by the buoyancy. Their wave-like domain is confined between hyperboloids, as shown in figure 5b. Outside the hyperboloid volume, these waves at the sub-harmonic resonance are evanescent (in global models). The characteristic curve delimiting the wave-like and evanescent domains is hyperbolic and given by equation (21). Along the polar axis, local waves at the sub-harmonic resonance do not propagate in the evanescent regions for vertical positions z_c satisfying

$$|z_c| \geq \frac{|1 - \bar{\Omega}_0|}{N_0/\Omega_s}. \quad (26)$$

This shows that an axial stratification has a stabilising effect, as predicted by formula (20).

This behaviour is responsible for an equatorial trapping of the waves in the other directions at the sub-harmonic resonance. Indeed, the hyperbolic wave-like domain, bounded by equation (21), converges towards the conical volume delimited by the asymptote $\cos(\theta_c) = |1 - \bar{\Omega}_0|/2$ (Friedlander & Siegmann 1982a), where θ_c is the critical colatitude. This is exactly formula (25). Therefore, expression (25) also defines the position of the critical latitudes at which the waves at the sub-harmonic resonance propagate orthogonally to the gravity field (here radial direction at the leading order in β_0). Hence, these specific waves are insensitive to the stratification. We emphasise that the presence of stratification does not alter the position of the critical latitudes (Friedlander & Siegmann 1982a,b). When $|1 - \bar{\Omega}_0| \rightarrow 0$, the waves at the sub-harmonic resonance are equatorially trapped according to formula (25).

3.3.3 Forbidden zone

Within the forbidden zone $\Omega_0 \leq -1$ and $\Omega_0 \geq 3$, any tidal instability must involve gravito-inertial waves \mathcal{E} for the sub-harmonic mechanism, whatever the strength of the stratification. Indeed, figure 4 clearly shows that the waves at the sub-harmonic resonance depend only on the value of the orbital frequency Ω_0 . When $N_0/\Omega_s \leq 1$, the sub-harmonic condition is never satisfied within this orbital range. Hence, no tidal instability is triggered. This is in agreement with formula (17) for the growth rate in the equatorial plane.

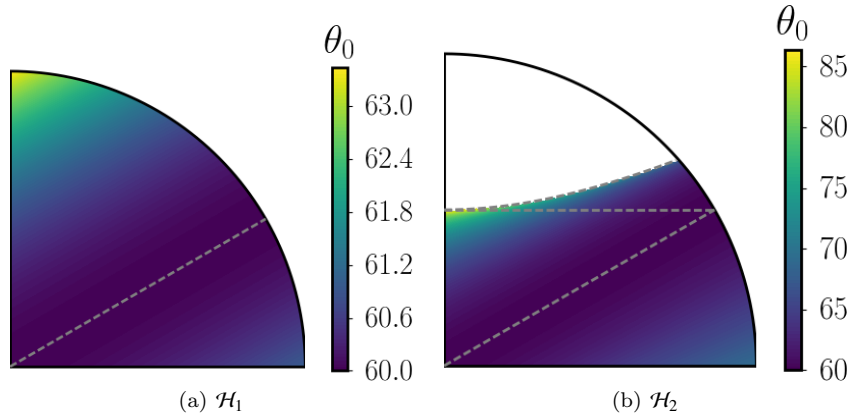


Figure 5. Wave-like domains and colatitude θ_0 (degrees) for the waves with hyperbolic turning surfaces \mathcal{H} satisfying sub-harmonic resonances. (a) \mathcal{H}_1 wave: $\Omega_0 = 0$, $N_0/\Omega_s = 0.5$. (b) \mathcal{H}_2 wave: $\Omega_0 = 0$, $N_0/\Omega_s = 2$. The dashed grey hyperbolic curve is given by equation (21). The tilted dashed grey line is the asymptote given by $\cos \theta_0 = |1 - \Omega_0|/2$. Waves disappear along the polar axis when $z \leq |1 - \Omega_0|/(N_0/\Omega_s)$.

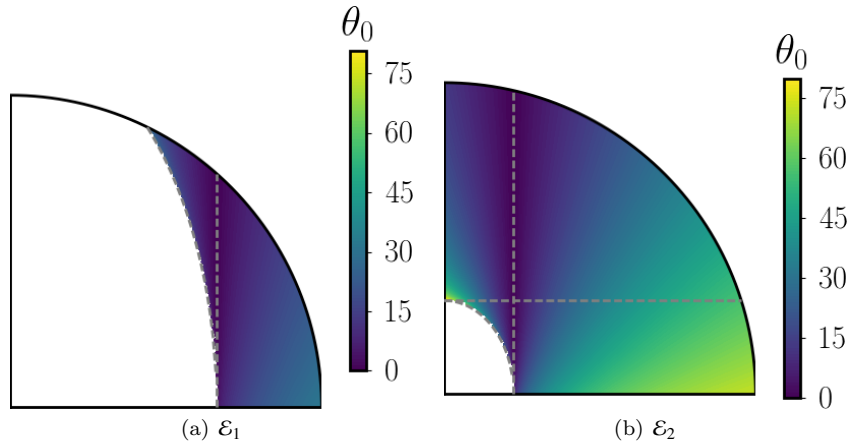


Figure 6. Wave-like domains and colatitude θ_0 (degrees) for the waves with ellipsoidal turning surface \mathcal{E} satisfying sub-harmonic resonances. (a) \mathcal{E}_1 wave: $\Omega_0 = 3.4$, $N_0/\Omega_s = 2$. (b) \mathcal{E}_2 wave: $\Omega_0 = 4$, $N_0/\Omega_s = 10$. The dashed grey ellipsoidal curve is given by equation (21). The vertical dashed grey line is the asymptote given by $s = \sqrt{|1 - \Omega_0|^2 - 4}/(N_0/\Omega_s)$, where s is the cylindrical radius from the spin axis. Waves disappears along the polar axis when $z \leq |1 - \Omega_0|/(N_0/\Omega_s)$.

However, gravito-inertial waves \mathcal{E} can be excited at the sub-harmonic resonance for a stronger stratification, typically $N_0/\Omega_s \gg 1$ when $|\Omega_0|$ increases. Their critical characteristic surfaces, given by equation (21), are ellipsoidal. On the one hand, \mathcal{E}_1 gravito-inertial waves are trapped in a region that does not encompass the polar axis, as shown in figure 6a. The minimum distance between the spin axis and the wave-like domain in the equatorial region is given by (Friedlander & Siegmann 1982a)

$$x_c = \frac{\sqrt{|1 - \Omega_0|^2 - 4}}{N_0/\Omega_s}. \quad (27)$$

Therefore, the thickness of the wave-like domain increases when the ratio N_0/Ω_s increases. On the other hand, \mathcal{E}_2 waves at the sub-harmonic resonance are gravito-inertial waves, trapped in a region that excludes the central part of the fluid (figure 6b). Along the polar axis, these waves do not propagate when z is smaller than the critical value (26). The size of wave-like domain increases when the ratio N_0/Ω_s increases. In the limit $N_0/\Omega_s \rightarrow \infty$, these waves become almost pure internal gravity waves, propagating in the whole fluid domain at the sub-harmonic resonance. This situation has

been investigated numerically in local models (Le Reun et al. 2018), by assuming $\Omega_s = 0$.

3.4 Growth rate in the orbital range $-1 \leq \Omega_0 \leq 3$

The necessary condition for instability (9), illustrated in figure 4, exactly coincides with the unstable zones of the tidal instability in the equatorial plane (see figure 3). However, it does not predict the growth rate σ of the instability. To go beyond the analytical formulas in the equatorial and polar regions, we solve numerically the local stability equations (11). We have used the local stability code SWAN (<https://bitbucket.org/vidalje/swan/>), introduced in Vidal & Cébron (2017). We have updated it to handle the general local stability equations, which are described in appendix C. Moreover, by solving numerically the full local equations, we do not assume a priori the sub-harmonic condition (9). Hence, we can assess the general validity of the sub-harmonic condition (9) in stratified fluids, as already found in (Kerswell 1993a, 1994; Le Dizès 2000; Vidal & Cébron 2017).

In the astrophysical regime $\beta_0 \ll 1$, the resonance con-

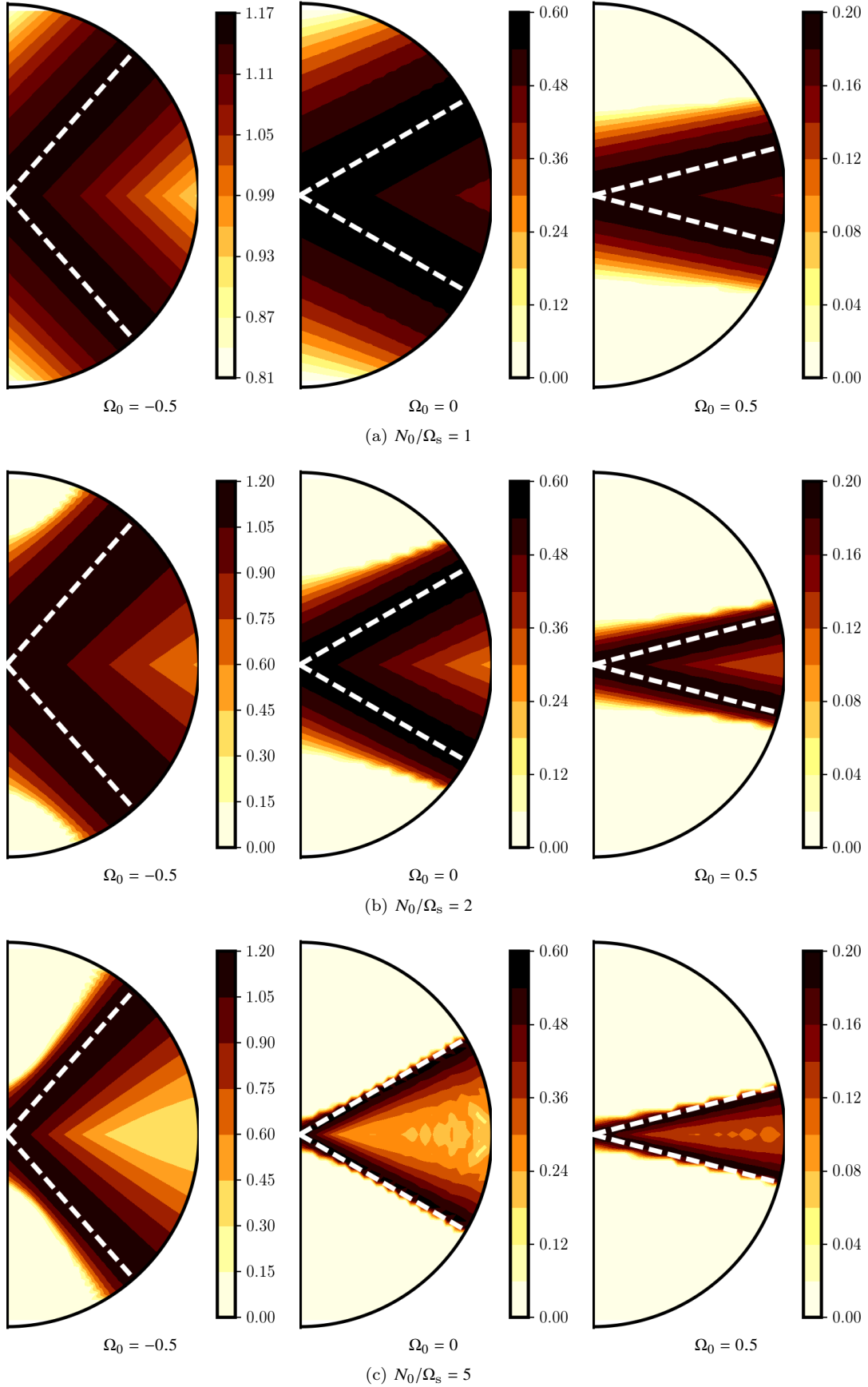


Figure 7. Largest normalised growth rate σ/β_0 for several configurations, computed with the SWAN code. Ellipsoidal boundary of ellipticity $\beta_0 = 0.2$. Visualisations in a meridional plane with normalised axes x/a and z/c , with $a = \sqrt{1 + \beta_0}$, $b = \sqrt{1 - \beta_0}$ and $c = 1/(ab)$. White dashed lines show the conical layers where the growth rates are maximum, as predicted by formula (25).

dition, either (8) or (9), is satisfied numerically for only a few initial wave vectors \mathbf{k}_0 . Numerically, this is too expansive to survey all the possible configurations for \mathbf{k}_0 . Thus, we set the equatorial ellipticity to the value $\beta_0 = 0.2$. This does not change in any way the relevance of the following numerical results, because σ is proportional to β_0 (when $\beta_0 \ll 1$). However, for large values of β_0 , the general resonance condition (8) can be satisfied for a wider range of initial wave vectors \mathbf{k}_0 , due to geometrical detuning effects (Le Dizès 2000; Vidal & Cébron 2017). Hence, the simulations are more tractable numerically. In practice, we have considered many fluid trajectories $\mathbf{X}(t)$ and \mathbf{k}_0 , sampling the whole ellipsoidal domain, to get representative results.

We have benchmarked the code against analytical formulas (16) and (20) in the equatorial and polar regions, obtaining a perfect agreement and cross-validating the asymptotic analysis (not shown). Then, we only investigate the stability of the equilibrium tide flow (7) within the orbital range $-1 \leq \Omega_0 \leq 3$, for which the binary systems considered in §5 belong. When the stratification is neutral ($N_0 = 0$), the whole domain is unstable (not shown) as expected, with a homogeneous growth rate predicted by formula (17). We survey illustrative stably stratified configurations $N_0/\Omega_0 \geq 0$ in figure 7. Several aspects the figure are worthy of comment. We clearly recover the trapping of the instability by the axial stratification, outlined by the weakening of the growth rate in formula (20). In the bulk, the weakening first occurs in the polar regions, and then spreads out towards lower latitudes when N_0/Ω_s increases (from top to bottom panels in figure 7). Along the polar axis, it turns out that the transition between unstable and stable areas occurs at the position (26). In addition, the equatorial region is still unstable for the range of N_0/Ω_s considered, in agreement with figure 3.

Then, the numerical analysis unravels an unexpected feature compared to the asymptotic analysis. When N_0/Ω_s increases, tidal instabilities are always triggered in the bulk. The stratification confines the instabilities along conical layers (white dashed lines), tilted from the spin (polar) axis. The tilt angle is exactly the colatitude angle θ_0 , given by formula (25), which maximises the classical tidal instability for neutral fluids ($N_0 = 0$). This shows the equatorial trapping does not affect similarly all the orbits. When $-1 \leq \Omega_0 \leq 1$, the tilt angle θ_0 given by formula (25) goes from $\theta_0 = 0$ to $\theta_0 = \pi/2$. Hence, the instability on retrograde orbits (with small values of θ_0) is less significant than on prograde orbits. When $N_0/\Omega_s \gg 1$, the tidal instability is equatorially trapped between the conical layers, with growth rates on the equatorial plane predicted by formula (16). However, on these conical layers, it turns out that the largest growth rate σ is unaffected by the stratification, for any value of N_0/Ω_s . Hence, the maximum growth rate of the tidal instability in stratified fluids is always given by formula (17), for any orbit in the orbital range $-1 \leq \Omega_0 \leq 3$.

Therefore, the numerical analysis has confirmed and extended the asymptotic analysis. In stably stratified interiors, the tidal instability is triggered by sub-harmonic resonances of inertia-gravity waves in the orbital range $-1 \leq \Omega_0 \leq 3$. There is an equatorial trapping of the tidal instability between conical layers, depending on the orbital configuration according to formula (25). Yet, the maximum growth rate is unaffected by the stable stratification. Moreover, it turns out

that the sub-harmonic condition (9) is a necessary and sufficient condition for the existence of the tidal instability. Indeed, we have not found any other resonance yielding larger growth rates compared to the sub-harmonic resonances.

3.5 Magnetic effects

We reintroduce now the leading-order effects of the pervading magnetic fields at the onset of the tidal instability. We have already shown that a magnetic field only weakly modifies the fast MAC waves at the sub-harmonic resonance, as illustrated by the spectrum 2. This is in agreement with global dynamo simulations, in homogeneous (Cébron & Hollerbach 2014; Reddy et al. 2018) and stratified fluids (Vidal et al. 2018), showing that even a dynamo magnetic field only barely modifies the hydrodynamic tidal flows. However, at the linear onset of the tidal instability, the Lorentz force introduces an Ohmic damping of the (diffusionless) growth rate (Herreman et al. 2009, 2010; Cébron et al. 2012b). Hence, the dimensionless growth rate σ ought to be reduced due to Joule diffusion by the Joule damping rate $\tau_\Omega \leq 0$. This Joule damping rate can be estimated by the damping rate of the free waves involved in the triadic resonances (8). Indeed, triadic couplings can only yield non-vanishing growth rates if the hydromagnetic waves individually exist, i.e. if they are not damped by Joule diffusion.

The pervading fossil magnetic fields are nearly axisymmetric and dipole-dominated at the leading order, as observed in magnetic binaries (e.g. Alecian et al. 2016; Landstreet et al. 2017; Kochukhov et al. 2018; Shultz et al. 2017, 2018). For the stability theory, the background fossil field is $\mathbf{B}_0 \propto \mathbf{1}_z$, with a dimensionless strength measured by the Lehnert number Le . The presence of other field components only slightly modifies the frequencies of the fast hydromagnetic waves, such that there is no reason to suggest that the damping rate would behave otherwise. In the regime $Le \ll 1$, the damping rates have been devised by Sreenivasan & Narasimhan (2017) in the local theory and by Kerswell (1994) in ellipsoidal geometry. It turns out that they depend on the wave properties at the resonance. Notably, we explain in appendix D why the mixed couplings between fast and slow MAC waves cannot lead to any tidal instability in close-binaries. Hence, only sub-harmonic resonances of fast MAC waves can generate the tidal instability in the presence of magnetic fields.

Following Sreenivasan & Narasimhan (2017), the Joule damping rate of the fast waves is, at the leading order in $Le \ll 1$,

$$\frac{\tau_\Omega}{|1 - \Omega_0|} = -\frac{\cos^2(\theta_0) |\mathbf{k}_0|^4 Em Le^2}{4 \cos^2(\theta_0) + |\mathbf{k}_0|^4 Em^2} \quad (28)$$

with $|\mathbf{k}_0|$ the norm of the wave vector at the resonance (and at initial time) and $\cos(\theta_0)$ given by condition (25). Note that formula (28) is exactly the Joule decay rate of the tidal instability in homogeneous fluids (Herreman et al. 2009; Cébron et al. 2012b). Formula (28) has two asymptotic behaviours, depending on the value of \mathbf{k}_0 . They are separated by the condition

$$|\mathbf{k}_0| = \sqrt{2 \cos(\theta_0) / Em} \sim Em^{-1/2}. \quad (29)$$

On the one hand, we obtain a wave-dominated regime when $|\mathbf{k}_0| \leq Em^{-1/2}$, in which the Joule damping rate scales as

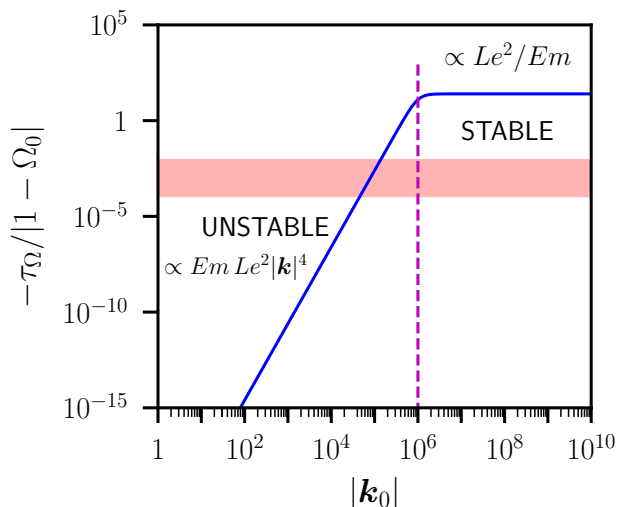


Figure 8. Dimensionless Joule damping $-\tau_{\Omega}/|1-\Omega_0|$ of the tidal instability (solid blue line) as a function of the magnitude of the wave number $|\mathbf{k}_0$. Dashed magenta line is given by formula (29), delimiting the two hydromagnetic regimes. Red shaded areas show the typical strength of the diffusionless growth rate of the tidal instability $\sigma \sim \mathcal{O}(\beta_0)$, with $\beta_0 \in [10^{-4}, 10^{-2}]$ for close binaries. Computations at $Le = 10^{-5}$ and $Ek/Pm = 10^{-12}$ for a dimensionless fossil field $\mathbf{B}_0 = \mathbf{1}_z$ aligned with the spin axis.

$\tau_{\Omega} \propto -Em Le^2 |\mathbf{k}_0|^4 / 4$. On the other hand, we get a diffusion-dominated regime when $|\mathbf{k}_0| \geq Em^{-1/2}$. In the latter regime, the damping rate is independent of the wave vector and scales as $\tau_{\Omega} \propto -Le^2/Em$. We illustrate in figure 8 the evolution of the Joule damping rate (28) in the different regimes. The tidal instability will survive in the presence of magnetic fields if $\sigma \gg |\tau_{\Omega}|$. Typical values of the diffusionless growth rate, given by formula (17), are $\sigma \sim \mathcal{O}(\beta_0)$ with $\beta_0 \in [10^{-4}, 10^{-2}]$ in close binaries. We clearly observe that the tidal instability does survive against Joule diffusion, for short-wavelength perturbations with $|\mathbf{k}_0| \leq 10^5$. For larger values of the wave number, the Joule damping rates always overcome the diffusionless growth rates, such that no instability is triggered.

Thus, in the astrophysical regime $Le \ll 1$, we have shown that the tidal instability can be triggered, even in the presence of fossil fields in close binaries. The underlying mechanism is the sub-harmonic resonance of fast hydromagnetic waves.

4 TIDAL MIXING

At this stage, we have shown that nonlinear tides can sustain the tidal instability in stably stratified interiors, even against the stabilising effects of the density stratification and magnetic fields. The next step is to characterise the saturated regime of the tidal flows. Modelling turbulent mixing in radiative interiors is one of the enduring problems in stellar dynamics (e.g. Zahn 1974). Several studies have examined the turbulence in radiative interiors (e.g. Zahn 1992; Mathis et al. 2004; Garaud et al. 2017; Gagnier & Garaud 2018; Mathis et al. 2018). Yet, these models only account

for shear-driven turbulence. Hence, the tidally driven turbulence in binaries remains to be described.

In homogeneous fluids, numerical simulations have shown that small-scale turbulence can be excited by tides (Le Reun et al. 2017), possibly leading to global tidal mixing (Vidal et al. 2018). Thus, tidal mixing is expected in radiative interiors. However, simulating this problem is severely hampered by the fact that any numerical model cannot probe accurately the stellar conditions. This makes the relevance of numerical results elusive. Therefore, we aim to build asymptotic scaling laws of the tidal mixing, based on dimensional-type arguments, that can embrace both numerical and stellar conditions.

In §4.1, we introduce the assumptions for our mixing-length theory of the tidal mixing. Then, we propose phenomenological prescriptions in §4.2, characterising the rotating stratified turbulence in the orbital range $-1 \leq \Omega_0 \leq 3$. Finally, we assess their validity by using proof-of-concept simulations in §4.3.

4.1 Mixing-length theory

4.1.1 Assumptions

We develop a phenomenological description of the nonlinear tidal mixing in radiative interiors, by using dimensional-type arguments. We employ a mixing-length theory to predict the mixing of the fossil field \mathbf{B}_0 . As shown in §3, magnetic effects play a minor role on the instability in the orbital range $-1 \leq \Omega_0 \leq 3$. They essentially damp out the growth rate of the instability (at the leading order). This is in agreement with dynamo nonlinear simulations of tidal flows in homogeneous (Cébron & Hollerbach 2014) and stratified fluids (Vidal et al. 2018). Indeed, the kinetic energy of the nonlinear tidal flows is largely unaffected by dynamo magnetic effects, even though they are essential for the self-sustained generation of the dynamo magnetic field. Therefore, we can reasonably switch off the Lorentz force $(\mathbf{B} \cdot \nabla)\mathbf{B}$ in the general momentum equation (2a). The nonlinear dynamics of the tidal flow is then uncoupled to the fossil field \mathbf{B}_0 . However, the nonlinear tides do mix the fossil field in induction equation (3c).

As commonly assumed in turbulent convection, any molecular diffusivity (denoted \mathcal{D}) is then replaced by an effective eddy diffusivity (denoted \mathcal{D}_t), induced by the nonlinear tides. By dimensional analysis (e.g. Tennekes & Lumley 1972), the mixing-length theory yields in dimensional form (up to a proportional constant)

$$\mathcal{D}_t \propto u_t l_t, \quad (30)$$

where u_t and l_t are respectively the typical (dimensional) velocity and length scale of the turbulent motions. The eddy diffusivity \mathcal{D}_t is a local property of the nonlinear flow, rather than a property of the fluid. The key point is to find accurate predictions for u_t and l_t .

On the one hand, we have shown in §3 that the tidal instability is generated by sub-harmonic resonances of inertial waves, more or less modified by the gravity field in the orbital range $-1 \leq \Omega_0 \leq 3$. This mechanism holds whatever the strength of the stratification, measured by the ratio N_0/Ω_s . This suggests that the turbulent velocity scale u_t should not depend on the strength of the local stratification (4), i.e. the

typical ratio N_0/Ω_s . This is supported by proof-of-concept simulations (see figure 2b of [Vidal et al. 2018](#)), showing that nonlinear tidal flows exhibit the scaling devised in homogeneous fluids ([Grannan et al. 2016](#)), i.e.

$$u_t \sim \beta_0 R \Omega_s (1 - \Omega_0), \quad (31)$$

Hence, we can safely estimate the turbulent velocity u_t by using prescription (31). On the other hand, l_t should depend on the local value of the stratification, i.e. the local ratio N/Ω_s . Indeed, several regimes have been found in forced stratified turbulence (e.g. [Brethouwer et al. 2007](#)).

4.2 Phenomenological prescriptions

4.2.1 Weakly stratified regime ($N_0/\Omega_s \leq 1$)

In the weakly stratified regime, characterised by $N_0/\Omega_s \leq 1$, \mathcal{H}_1 waves at the sub-harmonic resonance are barely affected by the stratification. This explains why the tidal mixing computed in [Vidal et al. \(2018\)](#) is constant, as long as $N_0/\Omega_s \leq 1$ (see their figure 9). We estimate l_t by balancing the nonlinear term $(\mathbf{u} \cdot \nabla)\mathbf{u}$ with the injection term $(\mathbf{u} \cdot \nabla)\mathbf{U}_0$ in momentum equation (3a). This leads to the typical turbulent length scale (in dimensional form) $l_t \sim R$. Hence, the eddy diffusivity in the weakly stratified regime reduces to the isotropic coefficient (in dimensional form)

$$\mathcal{D}_t \propto \beta_0 R^2 \Omega_s (1 - \Omega_0). \quad (32)$$

Prescription (32) shows that the eddy diffusivity is isotropic and should scale linearly with the equatorial ellipticity in the weakly stratified regime ($N_0/\Omega_s \leq 1$).

4.2.2 Stratified regimes ($N_0/\Omega_s \geq 1$)

We now investigate the stratified regimes $N_0/\Omega_s \geq 1$. Stratified turbulence is highly anisotropic. Indeed, a commonly observed feature of strongly stratified flows is the formation of quasi-horizontal layers, often described as pancake structures (e.g. [Billant & Chomaz 2001](#)). Such layers are conspicuous in simulations of tidal flows in strongly stratified fluids, both in non-rotating ([Le Reun et al. 2018](#)) and rotating fluids ([Vidal et al. 2018](#)). Hence, l_t depends on both the direction and the strength of the stratification. We introduce two turbulent length scales, respectively l_t^\parallel in the normal direction (i.e. along the gravity field) and l_t^\perp in the other horizontal directions.

Several regimes of stratified turbulence have been devised in fundamental fluid mechanics ([Billant & Chomaz 2001](#); [Brethouwer et al. 2007](#)). They are characterised by the buoyancy Reynolds number

$$\mathcal{R} \sim \frac{u_t^3}{l_t^\perp N_0^2 \nu}. \quad (33)$$

[Le Reun et al. \(2018\)](#) investigated the small-scale turbulence sustained by the tides in the regime $\mathcal{R} \leq 1$, in which vertical viscous shearing is important. However, radiative interiors are likely in the opposite regime $\mathcal{R} \gg 1$ ([Mathis et al. 2018](#)). Moreover, they neglected the rotation, by setting $\Omega_s = 0$. In such a configuration, the subspaces of waves $[\mathcal{H}_1, \mathcal{H}_2]$ at the sub-harmonic resonance are empty, according to dispersion relations (22). Hence, the associated tidal instability involves

only sub-harmonic resonances of internal waves \mathcal{H}_2 in the limit $N_0/\Omega_s \rightarrow \infty$ and $|\Omega_0| \rightarrow \infty$. Therefore, their results do not apply for our astrophysical problem, for any orbit in the range $-1 \leq \Omega_0 \leq 3$. In the relevant strongly stratified regime $\mathcal{R} \gg 1$, diffusion is unimportant and the turbulence is three-dimensional ([Brethouwer et al. 2007](#)). The general scalings of this regime have been confirmed by turbulence simulations (e.g. [Godeferd & Staquet 2003](#); [Maffioli & Davidson 2016](#)). Thus, they can be applied to the tidal problem. In addition, rotational effects are also important within the orbital range $-1 \leq \Omega_0 \leq 3$, even for large values of $N_0/\Omega_s \geq 10$. Hence, the resulting turbulence undergoes the combined action of stratification and rotation.

In rotating stratified turbulence, the two turbulent length scales are related by (e.g. [Billant & Chomaz 2001](#))

$$l_t^\perp \sim \frac{N_0}{\Omega_s} l_t^\parallel. \quad (34)$$

Turbulent scaling (34) has been confirmed in local simulations of rotating stratified turbulence ([Waite & Bartello 2006](#)). For strong stratification $N_0/\Omega_s \geq 10$, we combine the two balances obtained by equating (i) the nonlinear term with the buoyancy force in momentum equation (3a) and (ii) the injection term $(\mathbf{u} \cdot \nabla)\mathbf{T}_0$ and the nonlinear term $(\mathbf{u} \cdot \nabla)\Theta$ in energy equation (3b). These balances yield respectively

$$\frac{u_t}{l_t^\parallel} \sim \alpha_T g_0 \Theta_t \quad \text{and} \quad \alpha_T g_0 \Theta_t \sim N_0^2 l_t^\parallel, \quad (35)$$

where Θ_t is the typical dimensional turbulent buoyancy perturbation. From balances (35) we recover the classical scaling for the turbulent length scale in the normal direction, i.e. $u_t \sim l_t^\parallel N_0$ (e.g. [Billant & Chomaz 2001](#); [Brethouwer et al. 2007](#)). Hence, the turbulent length scale in the normal direction is

$$l_t^\parallel \sim \beta_0 R (1 - \Omega_0) \frac{\Omega_s}{N_0}. \quad (36)$$

Scaling (36) shows that tidal mixing falls in the asymptotic regime of strongly stratified turbulence ([Brethouwer et al. 2007](#)). Then, we obtain two prescriptions for the eddy diffusivity, the first one valid in the normal direction \mathcal{D}_t^\parallel and the second one \mathcal{D}_t in the perpendicular directions. They yield

$$\mathcal{D}_t^\parallel \propto \beta_0^2 R^2 \Omega_s (1 - \Omega_0)^2 \frac{\Omega_s}{N_0}, \quad (37a)$$

$$\mathcal{D}_t^\perp \propto \beta_0^2 R^2 \Omega_s (1 - \Omega_0)^2. \quad (37b)$$

Prescriptions (37) show that the eddy diffusivity should have a quadratic dependence with the equatorial ellipticity in any spatial direction. Another interesting prediction in this regime is that the turbulent potential and kinetic energies, defined by (in dimensional variables)

$$E_t(\Theta^*) \sim \frac{1}{2} \frac{\alpha_T^2 g_0^2}{N_0^2} \Theta_t, \quad E_t(\mathbf{u}^*) \sim \frac{1}{2} u_t^2, \quad (38)$$

are of the same order of magnitude ([Billant & Chomaz 2001](#)). This can be checked in the numerical simulations (see later).

In-between the aforementioned two stratified regimes, i.e. when $1 \leq N_0/\Omega_s \leq 10$, the situation is unclear. Indeed, [Vidal et al. \(2018\)](#) found that $\mathbf{u} \cdot \mathbf{g}$, which is responsible for the normal tidal mixing, is largely unaffected by the stratification when $N_0/\Omega_s \leq 10$ (see their figure 4). This would

suggest to extend the prescription of the turbulent mixing (32) up to $N_0/\Omega_s \leq 10$. Yet, this behaviour is not conspicuous in the numerics (see figure 9b of Vidal et al. 2018). We propose that this may be due to the rather specific numerical method, which inaccurately probes the intermediate regime $1 \leq N_0/\Omega_s \ll 10$. Thus, we may expect also a transition between the two regimes (32) and (37) when $1 \leq N_0/\Omega_s \leq 10$.

4.3 Validation against simulations

4.3.1 Proof-of-concept methodology

We assess the relevance of predictions (32) and (37) by using direct numerical simulations. As explained in §4.1, the Lorentz force plays a negligible role on the flow dynamics for the tidal instability. Therefore, the dimensionless governing equations in the numerical model reduce to

$$\frac{\partial \mathbf{b}}{\partial t} = \nabla \times [(U_0 + \mathbf{u}) \times \mathbf{b}] + \frac{Ek}{Pm} \nabla^2 \mathbf{b}, \quad (39a)$$

$$\nabla \cdot \mathbf{b} = 0, \quad \mathbf{b}(\mathbf{r}, t = 0) = \mathbf{B}_0(\mathbf{r}), \quad (39b)$$

where the fossil field $\mathbf{B}_0(\mathbf{r})$ is imposed as an initial condition for the magnetic field perturbation $\mathbf{b}(\mathbf{r}, t)$. In equation (39a), the nonlinear flow \mathbf{u} is governed by the (decoupled) momentum and energy equations (3a)-(3b) without the Lorentz force. For the simulations, the governing equations are supplemented by the stress-free conditions

$$\mathbf{u} \cdot \mathbf{1}_n = 0, \quad \mathbf{1}_n \times [(\nabla \mathbf{u} + (\nabla \mathbf{u})^\top) \mathbf{1}_n] = \mathbf{0}, \quad (40)$$

and a fixed temperature perturbation $\Theta = 0$ at the boundary. Stress-free conditions (40) are known to lead to spurious numerical behaviours, associated with the evolution of angular momentum in weakly deformed spheres (Guermond et al. 2013). To solve this numerical issue, we follow Cébron & Hollerbach (2014) and Vidal et al. (2018) by imposing a zero-angular momentum for the velocity perturbation. Finally, the external region is assumed to be electrically insulating, such that the magnetic field \mathbf{b} matches a potential field at the boundary.

For the numerical simulations, we employ the proof-of-concept approach introduced in Vidal et al. (2018). Briefly, the reference ellipsoidal configuration (described in §2.3) is approximated in spherical geometry by an spatially varying equatorial ellipticity profile $\epsilon(\mathbf{r}, \beta_0)$, depending of the ellipticity β_0 of the ellipsoidal configuration. This profile is chosen such that the reference configuration satisfies all the aforementioned boundary conditions in the spherical geometry. We refer the reader to Vidal et al. (2018) for further methodological details.

In magnetic radiative stars, the topology of the fossil field $\mathbf{B}_0(\mathbf{r})$ is not arbitrary. Indeed, only magnetic equilibria involving poloidal and toroidal components are stable (e.g. Braithwaite & Spruit 2017). However, the exact topology of the fossil field is not essential for our numerical model. Indeed, induction equation (39a) is not coupled to the momentum equation (negligible Lorentz force). Thus, problem (39) is a kinematic (i.e. linear) initial value problem for the fossil field. By linearity, all the components of the fossil field can be considered independently. For each magnetic component, we can then measure a typical global turbulent eddy diffusivity (30).

To do so, we compute the (dimensionless) decay rate

$\sigma_\eta \leq 0$ of the volume average of the magnetic energy over the computational integration time T , i.e.

$$\sigma_\eta = \lim_{T \rightarrow \infty} \frac{1}{T} \log \left(\int_{\mathcal{V}} \frac{1}{2} |\mathbf{b}|^2 d\mathcal{V} \right). \quad (41)$$

Decay rate (41) is a global estimate in the simulations of the effective diffusivity \mathcal{D}_t . Note that Käpylä et al. (2019) measured in a similar way the turbulent diffusivity, obtaining a good quantitative agreement with mean-field analyses.

The decay rate should have the same scaling law in β_0 for all the initial magnetic fields. Yet, the (arbitrary) prefactors will be different. Indeed, all the (separate) magnetic components may not obey the same scaling law in the strongly stratified regime. Notably, we expect toroidal magnetic fields, satisfying $\mathbf{B}_0 \cdot \mathbf{1}_n = 0$ (at any position), to be preferentially mixed in the normal direction. Thus, scaling (37a) should apply predominantly for toroidal fields. On the contrary, we expect poloidal magnetic fields (with predominant components in the normal direction) to obey scaling (37b). However, we emphasise that the prefactors obtained from numerical simulations, performed for conditions far-removed from the astrophysical regime, are likely irrelevant for the astrophysical problem. Hence, with our numerical method, only the dependence in β_0 can be safely validated against simulations. Hence, we should have (i) $\sigma_\eta \propto \beta_0$ in the weakly stratified regime (32) and (ii) $\sigma_\eta \propto \beta_0^2$ in the strongly stratified regime (37).

4.3.2 Numerical results

The simulations have been performed with the open-source nonlinear code XSHELLS (<https://nschaeff.bitbucket.io/xshells/>), described in Schaeffer et al. (2017) and validated against standard spherical benchmarks (Marti et al. 2014; Matsui et al. 2016). A second-order finite difference scheme is used in the radial direction. The angular directions are discretised using a pseudo-spectral spherical harmonic expansion, provided by the blazingly efficient SHTns library (Schaeffer 2013). The time-stepping scheme is of second order in time and treats the diffusive terms implicitly, while the nonlinear and Coriolis terms are handled explicitly.

As a reference configuration, we have assumed $\Omega_0 = 0$. Indeed, we have shown theoretically in §3 that the underlying mechanism of the tidal instability does not change in the range $-1 \leq \Omega_0 \leq 3$, and similarly the turbulent scalings (e.g. Grannan et al. 2016; Vidal et al. 2018). Hence, investigating only one orbital configuration is necessary. Then, we have chosen as an initial fossil field the least-damped, poloidal free decay magnetic mode of the sphere (see Moffatt 1978, p. 36-40). This particular magnetic field is an exact solution of the purely diffusive induction equation. It has the smallest Ohmic free decay rate σ_Ω (in dimensionless form), given by

$$\sigma_\Omega = \pi^2 Ek / Pm. \quad (42)$$

This is the most suited field to assess the validity of the turbulent scaling laws. Indeed, the slow Joule diffusion (42) should not be coupled with the expected faster turbulent diffusion. In practice, we conducted the simulations at the fixed dimensionless numbers $Ek = 10^{-4}$, $Pr = 1$ and $Pm =$

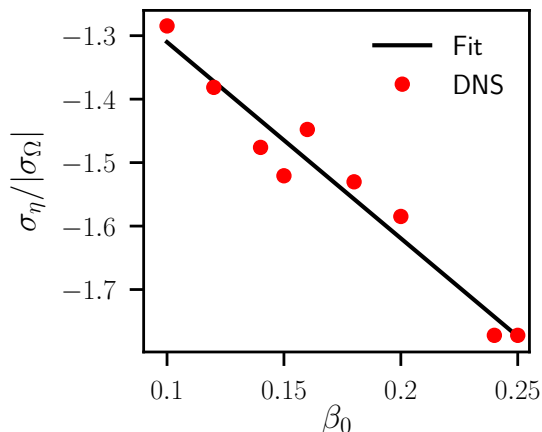
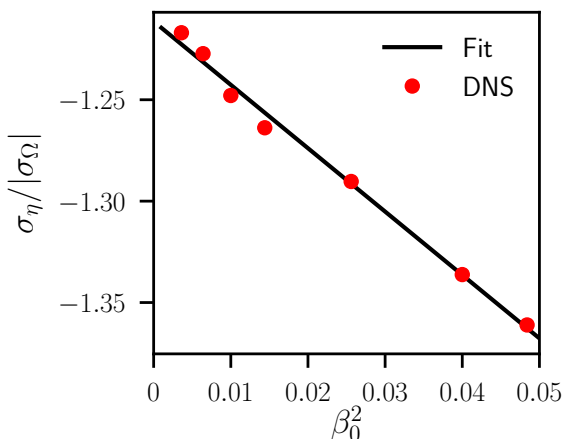
(a) Weakly stratified regime (e.g. $N_0/\Omega_s = 0$ here)(b) Strongly stratified regime (e.g. $N_0/\Omega_s = 10$ here)

Figure 9. Turbulent diffusion of magnetic fields by nonlinear tides. Ratio $\sigma_\eta/|\sigma_\Omega|$ of the global decay rate σ_η of the magnetic field \mathbf{b} , normalised by the free magnetic decay rate σ_Ω (Moffatt 1978) of the initial magnetic field \mathbf{B}_0 , as a function of the equatorial ellipticity β_0 . Simulations at $\Omega_0 = 0$, $Ek = 10^{-4}$, $Pr = 1$ and $Pm = 0.1$. The least-squares fits are $\sigma_\eta/|\sigma_\Omega| = -3.09\beta_0 - 1.00$ in (a) and $\sigma_\eta/|\sigma_\Omega| = -3.13\beta_0^2 - 1.21$ in (b).

0.1. The latter value ensures that no dynamo magnetic field can grow exponentially our spatial discretisation is $N_r = 224$ radial points, $l_{\max} = 128$ spherical harmonic degrees and $m_{\max} = 100$ azimuthal wave numbers. We have integrated the equations on one (dimensionless) Ohmic diffusive time $(Ek/Pm)^{-1}$ to determine accurately the turbulent decay rate σ_η .

Figure 9 shows the representative results for the two stratified regimes. We observe that the decay rate σ_η is always larger than the free decay rate σ_Ω expected for the initial fossil field. Then, the striking feature is that we recover the two scalings as a function of the ellipticity, predicted by our mixing-length theory. In the weakly stratified regime (figure 9a), the numerical eddy diffusivity (41) is in broad agreement with the linear scaling $\sigma_\eta \propto \beta_0$, consistent with the mixing-length formula (32). The agreement is even much

better in the strongly stratified regime (figure 9b), obtaining the quadratic scaling $\sigma_\eta \propto \beta_0^2$ expected from (37).

Finally, the typical ratio of the volume averaged thermal and kinetic (dimensionless) energies, for the simulations of figure 9b, is $E(\Theta)/E(\mathbf{u}) = 8.1 \pm 3.5$. This numerical value is in very good agreement with the theoretical scaling (38) in the strongly stratified regime (Billant & Chomaz 2001), yielding $E(\Theta)/E(\mathbf{u}) \sim N_0/\Omega_s = 10$ in dimensionless variables. This is another evidence of the validity of the mixing-length theory.

5 ASTROPHYSICAL DISCUSSION

We have obtained a consistent picture of the tidal instability in an idealised set-up of radiative interiors. It predicts the linear onset (§3) and the nonlinear mixing induced by the saturated flows (§4). For the sake of theoretical and numerical validations, we have only considered rather idealised stellar models, described in §2. Then, the predictions have been successfully confronted with proof-of-concept numerical simulations, paving the way for astrophysical applications.

Indeed, we emphasise that more relevant stellar conditions can be embraced. In particular, the sub-harmonic condition still holds by considering more realistic stratified configurations for the waves (Friedlander & Siegmund 1982a). Similarly, the mixing-length theory is only based on local dimensional arguments, that remain valid for more realistic conditions. Therefore, we discuss now our findings in the context of tidally deformed and stably stratified (radiative) interiors. Notably, we are in the position to build a new physical scenario, that may explain the lower incidence of fossil fields in short-period and non-synchronised binaries (Alecian et al. 2017).

5.1 A new scenario

We consider a close binary system with a radiative primary of mass M_1 and a secondary of mass M_2 . The primary is pervaded by an initial fossil field \mathbf{B}_0 . Note that distinction between the primary and secondary is only made for convenience, such that the situation can be reversed in the scenario (if we are interested in the secondary). The orbital and spin angular velocities are respectively Ω_{orb} and Ω_s . We focus on non-synchronised binaries in the orbital range $-1 \leq \Omega_0 \leq 3$, where $\Omega_0 = \Omega_{\text{orb}}/\Omega_s$ is the dimensionless orbital frequency. The orbits are almost circularised, but small orbital eccentricities $e \ll 1$ do not strongly modify the fate of tidal flows (Vidal & Cébron 2017). We also focus on binaries with short-period systems, with typical periods $T_s = 2\pi/\Omega_s \leq 10$ days. Due to the combined action of the tides and the spin, the star is deformed into an triaxial ellipsoid (Chandrasekhar 1969; Lai et al. 1993; Barker et al. 2016). The latter is characterised by a typical equatorial ellipticity β_0 , estimated from the static bulge theory (Cébron et al. 2012b; Vidal et al. 2018). For the bulge generated onto the primary, this reads

$$\beta_0 \sim \frac{3}{2} \frac{M_2}{M_1} \left(\frac{R}{D} \right)^3, \quad (43)$$

where R is the typical radius of the primary and D the typical distance separating the two bodies. The density strati-

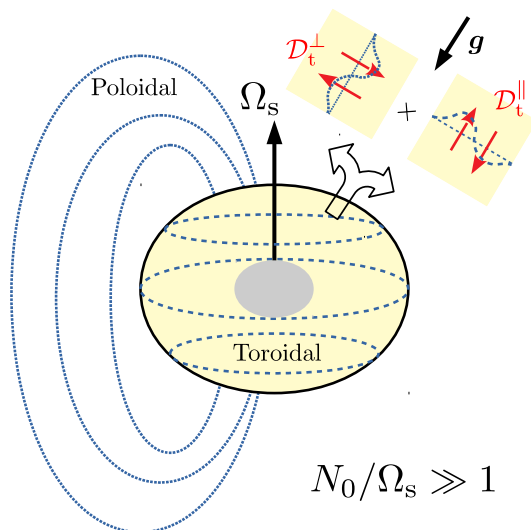


Figure 10. Anisotropic turbulent mixing of the poloidal (dotted) and toroidal (dashed) field lines of the fossil field \mathbf{B}_0 by the nonlinear tides. A possible innermost convective core is also represented.

fication of the radiative envelope is measured by the typical dimensionless ratio N_0/Ω_s , where N_0 is the typical Brunt-Väisälä frequency. A representative value for intermediate-mass stars is $N_0 \sim 10^{-3} \text{ s}^{-1}$ (e.g. Rieutord 2006), yielding a typical ratio $N_0/\Omega_s \gg 10$.

The tidal forcing sustains an equilibrium tidal velocity field (Remus et al. 2012; Vidal & Cébron 2017) in the primary fluid body. This equilibrium tidal flow can be nonlinearly coupled with free inertial-gravity waves, to trigger tidal instabilities. The dimensional growth rate σ^* of the tidal instabilities, which does not depend on the stratification, is given by

$$\sigma^* = \frac{(2\widetilde{\Omega}_0 + 3)^2}{16(1 + \widetilde{\Omega}_0)^2} |\Omega_s - \Omega_{\text{orb}}| \beta_0, \quad (44)$$

with $\widetilde{\Omega}_0 = \Omega_0/(1 - \Omega_0)$. In the saturated regime, the tidal instabilities enhance the internal mixing due to turbulence. In strongly stratified radiative interiors ($N_0/\Omega_s \gg 10$), the turbulent mixing generated by the nonlinear tides is anisotropic, characterised by an eddy turbulent diffusivity $\mathcal{D}_t^{\parallel}$ in the direction of the self-gravity and by $\mathcal{D}_t^{\perp} (\gg \mathcal{D}_t^{\parallel})$ in the other (horizontal) directions.

Then, the turbulent mixing will dynamically disrupt the fossil field \mathbf{B}_0 . However, the latter field, containing both poloidal and toroidal components (to be in quasi-static magnetic equilibrium in the initial stage), will undergo an anisotropic tidal disruption. The mechanism is illustrated in figure 10. On the one hand, the poloidal components, which are mainly along the normal direction and can be observed at the stellar surface, are preferentially disrupted by the (large) eddy diffusivity \mathcal{D}_t^{\perp} in the horizontal directions. On the other hand, the toroidal components, hidden in the star since they are only along the horizontal directions, are preferentially mixed by the (small) eddy diffusivity $\mathcal{D}_t^{\parallel}$ in the normal direction. Thus, poloidal and toroidal field lines are disrupted on different typical turbulent time scales. However, as soon as the fossil magnetic equilibrium

is disrupted (by the tidal flows), both poloidal and toroidal magnetic components quickly die out a few Alfvén time scales $(Le \Omega_s)^{-1}$, as shown theoretically and numerically (e.g. Tayler 1973; Markey & Tayler 1973, 1974; Braithwaite 2009; Mitchell et al. 2014). Therefore, the typical turbulent time scale for the tidal disruption of the fossil field is

$$\tau_t \propto \frac{R^2}{\mathcal{D}_t^{\perp}} = \frac{1}{\beta_0^2 \Omega_s (1 - \Omega_0)^2}, \quad (45)$$

i.e. the fast turbulent time scale in the perpendicular directions destroying the poloidal components.

5.2 Non-magnetic binaries

We assess here the relevance of the tidal scenario for short-period massive binary systems. Non-magnetic and non-synchronised ($\Omega_0 \neq 1$) binaries are given in table 2. They have been surveyed by the BinaMIcS collaboration (e.g. Alecian et al. 2017). The predictions of the tidal scenario for these binary systems are given in table 3. All these close binaries are rapidly rotating and undergo strong tidal effects in the two bodies, as measured by the large values of the ellipticity $\beta_0 \sim 10^{-2}$. Hence, the tides do trigger quickly the tidal instability, growing on the typical time scale $(\sigma^*)^{-1} \leq \mathcal{O}(10^3)$ years. This is much shorter than the lifetime of these stars, about $\tau_{\text{MS}} \sim 10^9$ years for a star of mass $M_1 = 2M_{\odot}$ on the main sequence. Hence, the tidal instability is likely present in these non-synchronised binaries.

Then, typical values for the turbulent time scale (45) are $\tau_t \in [10^2, 10^6]$ years, except for HD 32964 which is less affected by the nonlinear tides (smaller β_0). Hence, the tidal disruption of the initial fossil fields does occur on a very short time scale compared to the stellar lifetime, typically $\tau_t/\tau_{\text{MS}} \ll 10^{-3}$. This time scale (45) is also much smaller than the time scale for the Ohmic decay rate of the magnetic field in the absence of turbulence $\tau_{\Omega} \propto (\Omega_s Ek/Pm)^{-1}$, due to the slow Joule diffusion. As illustrated in figure 11, we get by $\tau_t/\tau_{\Omega} \ll 10^{-2}$ (except for HD 32964).

Therefore, nonlinear tides in non-synchronised may sustain the tidal disruption of fossil fields, on time scales much shorter than the stellar lifetime. This may explain the scarcity of significant magnetic fields at the surface of massive stars in close binaries.

5.3 Magnetic binaries

We give in table 4 the orbital properties of some scarce magnetic binaries, analysed by the BinaMIcS collaboration. They were already known to be magnetic, e.g. HD 98088 (Babcock 1958; Abt et al. 1968; Carrier et al. 2002), ϵ Lupi (Shultz et al. 2015) and HD 156324 (Alecian et al. 2014b). The aforementioned tidal scenario would suggest that (strong) magnetic fields may be anomalies in short-period massive binaries. However, their existence does not necessarily challenge the tidal scenario (a priori).

We note that HD 156324 and HD 98088 are synchronised. The fate of the tidal instability for synchronised orbits ($\Omega_0 = 1$) is discussed in appendix B. On the one hand, system HD 156324 is nearly circularised (Shultz et al. 2017), whereas non-circular orbits are required for the tidal mechanism to operate in synchronised systems. Hence, the tidal

Symbol (figure 11)	System	M_1 (M_\odot)	M_2 (M_\odot)	R (M_1) (R_\odot)	R (M_2) (R_\odot)	D (R_\odot)	T_s (M_1) (days)	T_s (M_2) (days)	T_{orb} (days)	Eccentricity e
◦	HD 23642	2.22	1.57	1.84	1.57	11.96	2.49	2.45	2.46	0.0
▽	HD 24133	1.39	1.31	1.78	1.49	5.042	0.827	0.783	0.80	0.0
△	HD 24909	3.53	1.72	2.47	1.53	10.59	1.8	1.8	1.74	7.4×10^{-2}
◀	HD 25638	14.3	10.7	8.91	6.70	23.97	3.01	2.76	2.70	0.0
▶	HD 25833	5.36	4.90	2.99	2.60	14.67	2.0	1.7	2.03	7.1×10^{-2}
○	HD 32964	2.63	2.57	1.95	1.92	22.90	5.57	5.55	5.52	8.4×10^{-2}
□	HD 34364	2.48	2.29	1.78	1.82	18.24	3.90	4.01	4.13	0.0
◇	HD 36486	24.0	8.40	16.5	6.50	43.00	6.24	2.13	5.73	0.11
⊙	HD 150136	62.6	39.5	13.1	9.54	38.00	2.9	2.7	2.67	0.0

Table 2. Physical and orbital characteristics of the non-synchronised and non-magnetic binary systems considered in this study, surveyed by the BinaMicS collaboration (e.g. [Alecian et al. 2017](#)). The masses [M_1, M_2] of the primary and the secondary bodies are given in Sun mass unit M_\odot . The typical stellar radius R (of either the primary or of the secondary) and the typical distance D between the two bodies is given in Sun radius unit R_\odot . The spin and orbital periods [T_s, T_{orb}] are expressed in days. They yield the spin and angular velocities [$\Omega_s = 2\pi/T_s, \Omega_{\text{orb}} = 2\pi/T_{\text{orb}}$]. Note that T_s has been estimated by assuming aligned spin-orbit systems. HD 23642: [Groenewegen et al. \(2007\)](#), HD 24133: [Clausen et al. \(2010\)](#), HD 24909: [Değirmenci \(1997\)](#), HD 25638: [Tamajo et al. \(2012\)](#), HD 25833: [Giménez & Clausen \(1994\)](#), HD 32964: [Makaganiuk et al. \(2011\)](#), HD 34364: [Nordstrom & Johansen \(1994\)](#), HD 36486: [Shenar et al. \(2015\)](#), HD 150136: [Mahy et al. \(2012\)](#).

System	β_0		σ^* (1/year)		τ_t (years)		τ_t/τ_Ω	
	Body 1	Body 2	Body 1	Body 2	Body 1	Body 2	Body 1	Body 2
HD 23642	3.87×10^{-3}	4.77×10^{-3}	1.03×10^{-2}	5.07×10^{-3}	5.27×10^5	2.29×10^6	4.86×10^{-4}	2.15×10^{-3}
HD 24133	6.21×10^{-2}	4.12×10^{-2}	1.46×10^0	6.11×10^{-1}	7.53×10^1	5.10×10^2	2.09×10^{-7}	1.49×10^{-6}
HD 24909	9.27×10^{-3}	9.28×10^{-3}	9.25×10^{-2}	9.26×10^{-2}	8.71×10^3	8.69×10^3	1.11×10^{-5}	1.11×10^{-5}
HD 25638	5.76×10^{-2}	4.39×10^{-2}	1.12×10^0	2.03×10^{-1}	2.97×10^1	1.20×10^3	2.26×10^{-8}	9.97×10^{-7}
HD 25833	1.16×10^{-2}	9.13×10^{-3}	4.78×10^{-2}	5.83×10^{-1}	3.23×10^4	3.38×10^2	3.70×10^{-5}	4.56×10^{-7}
HD 32964	9.01×10^{-4}	9.04×10^{-4}	7.89×10^{-4}	4.61×10^{-4}	4.06×10^7	1.20×10^8	1.67×10^{-2}	4.97×10^{-2}
HD 34364	1.29×10^{-3}	1.60×10^{-3}	1.14×10^{-2}	7.12×10^{-3}	3.18×10^5	7.48×10^5	1.87×10^{-4}	4.28×10^{-4}
HD 36486	2.97×10^{-2}	1.48×10^{-2}	2.20×10^{-1}	4.32×10^0	3.94×10^2	1.07×10^1	1.45×10^{-7}	1.16×10^{-8}
HD 150136	3.91×10^{-2}	3.76×10^{-2}	5.98×10^{-1}	7.53×10^{-2}	1.16×10^2	2.46×10^1	9.19×10^{-8}	2.09×10^{-8}

Table 3. Predictions of the tidal scenario for the close binaries described in table 2. For all these stars, we have taken as representative value for the dimensional Brunt-Väisälä frequency $N_0 = 10^{-3} \text{ s}^{-1}$ (e.g. [Rieutord 2006](#)). The equatorial ellipticity β_0 is given by expression (43). The dimensional growth rate σ^* is given by formula (44). The turbulent time scale of tidal disruption τ_t is given by formula (45). The molecular Ohmic diffusive time scale is $\tau_\Omega \propto (\Omega_s Ek/Pm)^{-1}$ (in dimensional units of Ω_s), with $Ek/Pm \sim 10^{-12}$.

System	M_1 (M_\odot)	M_2 (M_\odot)	R (M_1) (R_\odot)	R (M_2) (R_\odot)	D (R_\odot)	T_s (M_1) (days)	T_s (M_2) (days)	T_{orb} (days)	Eccentricity e	B_0^* (M_1) (kG)	B_0^* (M_2) (kG)
HD 156324	8.5	4.1	3.8	2.3	13.2	1.58	1.58	1.58	0.0	14	< 2.6
HD 98088	2.19	1.67	2.76	1.77	21.7	5.905	5.905	5.905	0.18	3.9	< 1.6
ϵ Lupi (corot)	8.7	7.3	4.7	3.8	29.2	2.30	2.5	4.56	0.277	0.9	0.6
ϵ Lupi (slow)	8.7	7.3	4.7	3.8	29.2	6.4	7.1	4.56	0.277	0.9	0.6
ϵ Lupi (fast)	8.7	7.3	4.7	3.8	29.2	0.40	0.32	4.56	0.277	0.9	0.6

Table 4. Physical and orbital characteristics of the magnetic binary systems surveyed by the BinaMicS collaboration ([Folsom et al. 2013](#); [Shultz et al. 2015, 2017, 2018](#)). The masses [M_1, M_2] of the primary and the secondary bodies are given in Sun mass unit M_\odot . The typical stellar radius R (of either the primary or of the secondary) and the typical distance D between the two bodies is given in Sun radius unit R_\odot . The spin and orbital periods [T_s, T_{orb}] are expressed in days. They yield the spin and angular velocities [$\Omega_s = 2\pi/T_s, \Omega_{\text{orb}} = 2\pi/T_{\text{orb}}$]. The typical surface magnetic field B_0^* , believed to be of fossil origin, is given in kiloGauss (kG) for the two components. HD 156324 and HD 98088 are synchronised systems (see appendix B), whereas ϵ Lupi system is not synchronised.

mechanism is not currently relevant for HD 156324. This may explain why the fossil field is still observed. On the other hand, HD 98088 is not circularised such that nonlinear tidal mixing is expected. However, as shown in appendix B, formula (45) for the typical turbulent time scale ought to be reduced in synchronised systems, such that $(1 - \Omega_0)^2 \sim \epsilon^2$

with $\epsilon \ll 2e$ is the dimensionless amplitude of the tidal forcing ([Goldreich & Mitchell 2010](#); [Cébron et al. 2012b](#); [Vidal & Cébron 2017](#)). Based on the accuracy of the measured periods in table 4, we may assume $\epsilon \leq 10^{-3}$, such that the turbulent time scale τ_t , given by formula (B5), is expected to be much larger in HD 98088 than for the systems of table 3 (for

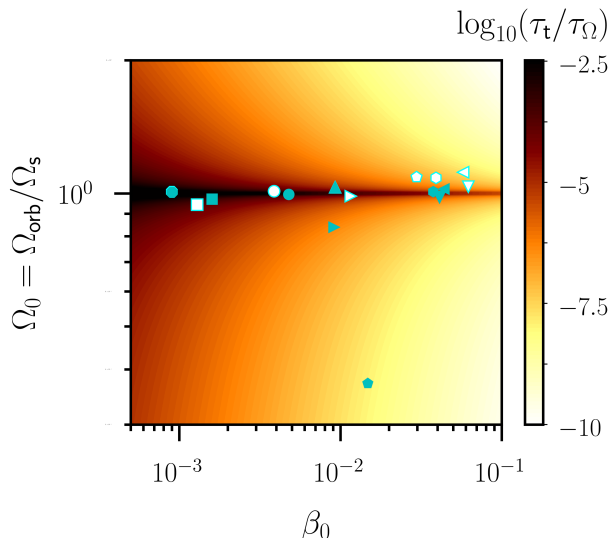


Figure 11. Turbulent decay of the fossil field τ_t (45), normalised by the typical Ohmic $\tau_\Omega \sim (\Omega_s Ek/Pm)^{-1}$, as a function of the equatorial ellipticity β_0 and the dimensionless orbital angular frequency $\Omega_0 = \Omega_{\text{orb}}/\Omega_s$. The close binaries of table 3 are illustrated by the symbols given in table 2. Large (white) symbols refer to the body 1 of the considered binary, whereas small (cyan) symbols refer to the body 2. Computations at $Ek/Pm = 10^{-12}$.

similar values of the equatorial ellipticity $\beta_0 \sim 10^{-3}$). Therefore, the existence of the (synchronised) magnetic binaries HD 156324 and HD 98088 appears to be consistent with the tidal scenario. However, note that the tidal mechanism may have occurred before the synchronisation and/or circularisation of the systems. Indeed, observations show that circularisation and synchronisation processes are effective for radiative stars (e.g. Giuricin et al. 1984a,b; Zimmerman et al. 2017). On the one hand, circularisation is expected to be faster in radiative stars, e.g. due to radiative damping (e.g. Zahn 1975, 1977). On the other hand, synchronisation processes have been much less studied in radiative interiors (e.g. Rocca 1989, 1987; Witte & Savonije 1999, 2001), and the confrontation with the observations is less satisfactory (e.g. Mazeh 2008; Zimmerman et al. 2017). Thus, understanding these two processes in radiative stars still deserves further work, notably to take into account the overlooked effects of the tidal instability in short-period binaries.

Finally, the case of ϵ Lupi system (e.g. Uytterhoeven et al. 2005; Shultz et al. 2015) is more intricate. Nonlinear tidal mixing should occur within these stars, with a short typical turbulent time scale $\tau_t \sim 10^3$ years. The fossil field may be currently disrupted by the nonlinear tides, but the process may have not last long enough to yield vanishing observable fields. Another possibility is that these magnetic fields would be internally regenerated by dynamo action, to balance the decay due to the nonlinear tides. Such a (currently speculative) mechanism may be particularly relevant for the rapidly rotating component of ϵ Lupi in table 4. Several dynamo mechanisms may be advocated, e.g. driven by differentially rotating flows (Braithwaite 2006), baroclinic flows (Simitev & Busse 2017) or even nonlinear tides (Vidal et al. 2018). Though the dynamo action of tides in strongly

stratified interiors remains elusive, the scaling law for the magnetic field strength at the stellar surface, proposed by Vidal et al. (2018), would yield $|\mathbf{B}_0| \sim 0.1 - 1$ kG. This is the order of magnitude of the observed surface fields. Thus, understanding the origin of the magnetic fields in the ϵ Lupi system certainly deserves future works.

6 CONCLUSION

6.1 Summary

In this work, we have investigated nonlinear tides in short-period massive binaries, motivated by the puzzling lower magnetic incidence of close binaries compared to isolated stars (Alecian et al. 2017; Alecian & et al. 2019). To do so, we have adopted an idealised model for rapidly rotating stratified fluids within the Boussinesq approximation, which are bounded in triaxial ellipsoids. This model consistently takes into account all the ingredients encountered in massive binaries, namely the combination of rotation and non-isentropic stratification, the tidal distortion (on coplanar and aligned orbits) and the leading-order magnetic effects. We have revisited the fluid instabilities triggered by the tides in the global system (Vidal et al. 2018), by combining analytical computations and proof-of-concept simulations.

First, we have investigated the linear onset of the tidal instability in non-synchronised, stratified fluid masses. Our results have unified all the previous existing stability analyses, within a single framework, and have unravelled new phenomena. We have shown that the tidal instability in radiative interiors is due to sub-harmonic resonances between inertial-gravity waves and the underlying equilibrium tidal flow, for any orbit in the range $-1 \leq \Omega_0 \leq 3$. Within this range, the tidal instability is weakened by a barotropic stratification along the polar axis (Miyazaki & Fukumoto 1991; Miyazaki 1993) and the equatorial plane. On the contrary, a baroclinic stratification does enhance the growth rate of the tidal instability (Kerswell 1993a; Le Bars & Le Dizès 2006). However, the striking feature is that the tidal instability onsets with a maximum growth rate which is unaffected by the stratification. The instability is triggered in volume along three-dimensional conical layers, whose position depends solely on the orbital parameter Ω_0 . In the orbital range $\Omega_0 \leq -1$ and $\Omega_0 \geq 3$, i.e. in the forbidden zone of the tidal instability in homogeneous fluids (e.g. Le Dizès 2000), the tidal instability can be generated by sub-harmonic resonances of gravito-inertial waves, provided that the stratification is strong enough for the considered orbital configuration. This provides a theoretical explanation of the instability mechanism investigated numerically in Le Reun et al. (2018).

Second, we have developed a predictive, mixing-length theory of the anisotropic tidal mixing, induced by nonlinear tides in the orbital regime $-1 \leq \Omega_0 \leq 3$. For strongly stratified interiors, we have modelled the anisotropic mixing by introducing two turbulent eddy diffusivities (e.g. Tennekes & Lumley 1972), one describing the mixing in the direction of the gravity field and the second in the other (horizontal) directions. We have shown that these two turbulent diffusivities should scale as β_0^2 , where β_0 is the equatorial ellipticity of the equilibrium tide. We have validated these scalings

against proof-of-concept simulations, by using the numerical method introduced in [Vidal et al. \(2018\)](#).

Finally, we have used the mixing-length theory to extrapolate the numerical results towards more realistic stellar conditions. We have built a new physical scenario, predicting the disruption of fossil fields by nonlinear tides in short-period (non-coalescing) massive binaries. We have applied it to a subset of short-period binaries, analysed by the BinaMIcS collaboration ([Alecian et al. 2017](#); [Alecian & et al. 2019](#)). This scenario may explain well the lower incidence of surface magnetic fields in short-period binaries than in isolated stars. Indeed, we predict a tidal disruption of fossil fields occurring in less than a few million years. This is much shorter than the Joule diffusion time scale of the fossil fields, and similarly than the typical lifetime of these stars.

6.2 Perspectives

This study calls for many improvements on the theoretical front, to confirm the likelihood of our mechanism. Since we have only handled the key ingredients, future works should strive to include additional effects within the model. First, it would be interesting to examine if (secondary) shear instabilities are sustained by the nonlinear tides in the strongly stratified regime. Shear instabilities are likely ubiquitous in radiative interiors (e.g. [Mathis et al. 2004, 2018](#)), which undergo differential rotations ([Goldreich & Schubert 1967](#)). To do so, the classical diffusionless instability condition for shear instabilities (e.g. [Drazin & Reid 1981](#)) ought to be modified in radiative interiors, to take into account the thermal diffusivity ([Townsend 1958](#); [Zahn 1974](#)). Hence, in the presence of turbulent tidally driven flows, secondary shear instabilities would exist if

$$Ri_t Pe_t \leq 1, \quad (46)$$

with $Ri_t = N_0^2/(u_t/l_t^\parallel)^2$ the turbulent Richardson number and $Pe_t = u_t l_t^\parallel / \mathcal{D}_t^\parallel$ the turbulent Péclet number. The typical estimate yields $Ri_t Pe_t \sim 1$ in the strongly stratified regime. Thus, such secondary shear instabilities may be triggered by the nonlinear tides, possibly enhancing the tidal mixing coefficient.

Then, a natural extension would be to investigate consistently the interplay between the dynamical tides and differential rotation, e.g. resulting from in-situ baroclinic torques (e.g. [Busse 1981, 1982](#); [Rieutord 2006](#)). However, we point out that this is unclear whether strong differential rotations can survive in the presence of fossil fields, because they are damped by hydromagnetic effects ([Arlt et al. 2003](#); [Rüdiger et al. 2013, 2015](#); [Jouve et al. 2015](#)). Nonetheless, the tidal elliptical instability does exist in differentially rotating elliptical flows, as shown in fundamental fluid mechanics ([Eloy & Le Dizès 1999](#); [Lacaze et al. 2007](#)). The properties of the modes in differentially rotating flows can be investigated in more realistic global models ([Friedlander 1989](#); [Mirouh et al. 2016](#)), such that extending the tidal theory seems achievable. Closely related to the study of differential rotation is the study of baroclinic flows (e.g. [Kitchatinov 2014](#); [Caleo & Balbus 2016](#); [Simitev & Busse 2017](#)). We have shown that baroclinic reference states do enhance the tidal instability, as first noticed by [Kerswell \(1993a\)](#) and [Le Bars](#)

& [Le Dizès \(2006\)](#). Thus, we may even expect a stronger turbulent tidal mixing in baroclinic radiative interiors.

Radiative stars also host innermost convective cores. Thus, the outcome of the tidal instability in shells should be considered. In shells, singular modes localised on attractors do exist ([Dintrans et al. 1999](#); [Mirouh et al. 2016](#); [Rieutord & Valdetaro 2018](#)). These singular modes are likely more affected by the magnetic field ([Lin & Ogilvie 2017](#)). However, we emphasise that almost regular modes do coexist with singular modes in shells (e.g. [Zhang 1993](#); [Vidal & Schaeffer 2015](#); [Barik et al. 2018](#)). The former can trigger tidal instabilities in shells, as confirmed experimentally and numerically for homogeneous fluids ([Aldridge et al. 1997](#); [Seyed-Mahmoud et al. 2000](#); [Lacaze et al. 2005](#); [Seyed-Mahmoud et al. 2004](#); [Lemasquier et al. 2017](#)). Moreover, the stability theory we have presented remains formally valid in shells. Hence, we do not expect any significant difference for stratified fluids at the onset. Then, the boundary effects on the turbulent tidal mixing remain to be determined.

Another daunting perspective is to account for compressibility. Using the Boussinesq approximation seems exaggerated for stellar interiors. However, the influence of the fluid compressibility is apparently negligible at the onset of the tidal instability ([Clausen & Tilgner 2014](#)). This is one of the reason why we have adopted the Boussinesq approximation. Moreover, investigating non-isentropic reference profiles cannot be easily simulated numerically with the more usual anelastic approximation (e.g. [Anufriev et al. 2005](#)). Clarifying the effects of compressibility certainly deserves future work, both in the linear and nonlinear regimes.

Finally, the scarce non-synchronised magnetic binaries ([Carrier et al. 2002](#); [Shultz et al. 2015](#); [Alecian et al. 2017](#); [Kochukhov et al. 2018](#)) seem to challenge the general trend of the tidal scenario, predicting a lack of magnetic massive stars in short-period binaries. These fields appear to be not disrupted by the nonlinear tides. If the tidal mechanism remains valid by including the aforementioned proposed improvements, they might be dynamically regenerated in situ by dynamo action. For instance, tides do sustain dynamo action in homogeneous fluids ([Cébron & Hollerbach 2014](#); [Reddy et al. 2018](#)), as well as in weakly stratified interiors ([Vidal et al. 2018](#)). Yet, the dynamo capability of tides remains elusive in strongly stratified interiors ([Vidal et al. 2018](#)). Baroclinic flows are a possible candidate, since they are dynamo capable ([Simitev & Busse 2017](#)). They may also favour the radial mixing generated by nonlinear tides, which is a necessary ingredient for dynamo action ([Kaiser & Busse 2017](#)). This certainly deserves future works to investigate dynamo magnetic fields in more realistic models of radiative stars.

ACKNOWLEDGEMENTS

JV was initially supported by a Ph.D grant from the French *Ministère de l'Enseignement Supérieur et de la Recherche* and later by STFC Grant ST/R00059X/1. DC was funded by the French *Agence Nationale de la Recherche* under grant ANR-14-CE33-0012 (MagLune) and by the 2017 TelluS program from CNRS-INSU (PNP) AO2017-1040353. AuD acknowledges support from NASA through Chandra Award number TM7-18001X issued by the Chandra X-ray Obser-

vatory Center, which is operated by the Smithsonian Astrophysical Observatory for and on behalf of NASA under contract NAS8- 03060. EA and the BinaMiCS collaboration acknowledges financial support from "Programme National de Physique Stellaire" (PNPS) of CNRS/INSU (France). JV acknowledges EA for inviting him at the BinaMiCS Workshop #5, from which came the idea to apply his theory of the tidal instability to explain the lack of magnetic binaries. AuD and EA acknowledge Dr S. Mathis (CEA, Paris Saclay) and the BinaMiCS collaboration for fruitful discussions. The authors kindly acknowledge Dr F. Gallet (IPAG, UGA) for having validated the typical estimate of the Brunt-Väisälä frequency in massive stars, by using a stellar evolution code. Computations were performed on the Froggy platform of CIMENT (<https://ciment.ujf-grenoble.fr>), supported by the Rhône-Alpes region (CPER0713 CIRA), OSUG2020 LabEx (ANR10 LABX56) and EquipMeso (ANR10 EQPX-29-01). ISTERre is also part of Labex OSUG@2020 (ANR10 LABX56). SWAN and SHINE codes are described at <https://bitbucket.org/vidalje/> and the XSHELLS code is freely available at <https://bitbucket.org/nschaeff/xshells>. Most figures were produced using matplotlib (<http://matplotlib.org/>).

REFERENCES

- Abt H. A., Conti P. S., Deutsch A. J., Wallerstein G., 1968, *The Astrophysical Journal*, 153, 177
- Akgün T., Reisenegger A., Mastrano A., Marchant P., 2013, *Monthly Notices of the Royal Astronomical Society*, 433, 2445
- Aldridge K., Seyed-Mahmoud B., Henderson G., van Wijngaarden W., 1997, *Physics of the Earth and Planetary Interiors*, 103, 365
- Alecian E., et al. 2019
- Alecian E., et al., 2014a, *Proceedings of the International Astronomical Union*, 9, 330
- Alecian E., et al., 2014b, *Astronomy & Astrophysics*, 567, A28
- Alecian E., Tkachenko A., Neiner C., Folsom C. P., Leroy B., 2016, *Astronomy & Astrophysics*, 589, A47
- Alecian E., Villebrun F., Grunhut J., Hussain G., Neiner C., Wade G. A., 2017, arXiv preprint arXiv:1705.10650
- Anufriev A. P., Jones C. A., Soward A. M., 2005, *Physics of the Earth and Planetary Interiors*, 152, 163
- Arlt R., Hollerbach R., Rüdiger G., 2003, *Astronomy & Astrophysics*, 401, 1087
- Aurieri M., et al., 2007, *Astronomy & Astrophysics*, 475, 1053
- Babcock H. W., 1958, *The Astrophysical Journal Supplement Series*, 3, 141
- Backus G., Rieutord M., 2017, *Physical Review E*, 95, 053116
- Bajer K., Mizerski K., 2013, *Physical Review Letters*, 110, 104503
- Barik A., Triana S. A., Hoff M., Wicht J., 2018, *Journal of Fluid Mechanics*, 843, 211
- Barker A. J., Braviner H. J., Ogilvie G. I., 2016, *Monthly Notices of the Royal Astronomical Society*, 459, 924
- Billant P., Chomaz J.-M., 2001, *Physics of Fluids*, 13, 1645
- Blazère A., Neiner C., Petit P., 2016, *Monthly Notices of the Royal Astronomical Society: Letters*, 459, L81
- Borra E. F., Landstreet J. D., Mestel L., 1982, *Annual Review of Astronomy and Astrophysics*, 20, 191
- Braithwaite J., 2006, *Astronomy & Astrophysics*, 449, 451
- Braithwaite J., 2009, *Monthly Notices of the Royal Astronomical Society*, 397, 763
- Braithwaite J., Cantiello M., 2012, *Monthly Notices of the Royal Astronomical Society*, 428, 2789
- Braithwaite J., Nordlund Å., 2006, *Astronomy & Astrophysics*, 450, 1077
- Braithwaite J., Spruit H. C., 2004, *Nature*, 431, 819
- Braithwaite J., Spruit H. C., 2017, *Royal Society Open Science*, 4, 160271
- Brethouwer G., Billant P., Lindborg E., Chomaz J.-M., 2007, *Journal of Fluid Mechanics*, 585, 343
- Brun A. S., Browning M. K., Toomre J., 2005, *The Astrophysical Journal*, 629, 461
- Busse F. H., 1981, *Geophysical & Astrophysical Fluid Dynamics*, 17, 215
- Busse F. H., 1982, *The Astrophysical Journal*, 259, 759
- Caleo A., Balbus S. A., 2016, *Monthly Notices of the Royal Astronomical Society*, 457, 1711
- Carrier F., North P., Udry S., Babel J., 2002, *Astronomy & Astrophysics*, 394, 151
- Cébron D., Hollerbach R., 2014, *The Astrophysical Journal Letters*, 789, L25
- Cébron D., Maubert P., Le Bars M., 2010, *Geophysical Journal International*, 182, 1311
- Cébron D., Le Bars M., Noir J., Aurnou J. M., 2012a, *Physics of Fluids*, 24, 061703
- Cébron D., Le Bars M., Moutou C., Le Gal P., 2012b, *Astronomy & Astrophysics*, 539, A78
- Cébron D., Le Bars M., Le Gal P., Moutou C., Leconte J., Sauret A., 2013, *Icarus*, 226, 1642
- Cébron D., Vantieghem S., Herreman W., 2014, *Journal of Fluid Mechanics*, 739, 502
- Chandrasekhar S., 1969, *Ellipsoidal figures of equilibrium*. Yale University Press
- Charbonneau P., 2014, *Annual Review of Astronomy and Astrophysics*, 52, 251
- Clausen N., Tilgner A., 2014, *Astronomy & Astrophysics*, 562, A25
- Clausen J. V., Olsen E. H., Helt B. E., Claret A., 2010, *Astronomy & Astrophysics*, 510, A91
- Commerçon B., Hennebelle P., Audit E., Chabrier G., Teyssier R., 2010, *Astronomy & Astrophysics*, 510, L3
- Commerçon B., Hennebelle P., Henning T., 2011, *The Astrophysical Journal Letters*, 742, L9
- Craik A. D. D., 1988, *Proceedings of the Royal Society of London A: Mathematical, Physical and Engineering Sciences*, 417, 235
- Craik A. D. D., 1989, *Journal of Fluid Mechanics*, 198, 275
- Craik A. D. D., Criminale W. O., 1986, *Proceedings of the Royal Society of London A: Mathematical, Physical and Engineering Sciences*, 406, 13
- Değirmenci İ. L., 1997, *Astrophysics and space science*, 253, 237
- Dintrans B., Rieutord M., Valdetaro L., 1999, *Journal of Fluid Mechanics*, 398, 271
- Drazin P. G., Reid W. H., 1981, *Hydrodynamic stability*. Cambridge University Press
- Duez V., Mathis S., 2010, *Astronomy & Astrophysics*, 517, A58
- Duez V., Braithwaite J., Mathis S., 2010, *The Astrophysical Journal Letters*, 724, L34
- Eloy C., Le Dizès S., 1999, *Journal of Fluid Mechanics*, 378, 145
- Fabijonas B. R., 2002, *Physics of Plasmas*, 9, 3359
- Favier B., Grannan A. M., Le Bars M., Aurnou J. M., 2015, *Physics of Fluids*, 27, 066601
- Featherstone N. A., Browning M. K., Brun A. S., Toomre J., 2009, *The Astrophysical Journal*, 705, 1000
- Finlayson B. A., 2013, *The method of weighted residuals and variational principles*. SIAM
- Folsom C. P., Likuski K., Wade G. A., Kochukhov O., Alecian E., Shulyak D., 2013, *Monthly Notices of the Royal Astronomical Society*, 431, 1513
- Friedlander S., 1987, *Geophysical & Astrophysical Fluid Dynamics*, 39, 315
- Friedlander S., 1989, *Geophysical & Astrophysical Fluid Dynamics*

- ics, 48, 53
- Friedlander S., Siegmann W. L., 1982a, *Geophysical & Astrophysical Fluid Dynamics*, 19, 267
- Friedlander S., Siegmann W. L., 1982b, *Journal of Fluid Mechanics*, 114, 123
- Friedlander S., Vishik M., 1990, *Geophysical & Astrophysical Fluid Dynamics*, 55, 19
- Friedlander S., Vishik M. M., 1991, *Physical Review Letters*, 66, 2204
- Friedlander S., Vishik M. M., 1995, *Chaos: An Interdisciplinary Journal of Nonlinear Science*, 5, 416
- Gagnier D., Garaud P., 2018, *The Astrophysical Journal*, 862, 36
- Garaud P., Gagnier D., Verhoeven J., 2017, *The Astrophysical Journal*, 837, 133
- Gastine T., Dintrans B., 2008a, *Astronomy & Astrophysics*, 484, 29
- Gastine T., Dintrans B., 2008b, *Astronomy & Astrophysics*, 490, 743
- Giménez A., Clausen J. V., 1994, *Astronomy and Astrophysics*, 291, 795
- Giuricin G., Mardirossian F., Mezzetti M., 1984a, *Astronomy and Astrophysics*, 131, 152
- Giuricin G., Mardirossian F., Mezzetti M., 1984b, *Astronomy and Astrophysics*, 135, 393
- Godeferd F. S., Staquet C., 2003, *Journal of Fluid Mechanics*, 486, 115
- Goldreich P. M., Mitchell J. L., 2010, *Icarus*, 209, 631
- Goldreich P., Schubert G., 1967, *The Astrophysical Journal*, 150, 571
- Grannan A. M., Favier B., Le Bars M., Aurnou J. M., 2016, *Geophysical Journal International*, 208, 1690
- Greenspan H. P., 1968, *The theory of rotating fluids*. Cambridge University Press
- Groenewegen M. A. T., Decin L., Salaris M., De Cat P., 2007, *Astronomy & Astrophysics*, 463, 579
- Grunhut J. H., et al., 2016, *Monthly Notices of the Royal Astronomical Society*, 465, 2432
- Gubbins D., Roberts P. H., 1987, *Geomagnetism*, 2, 1
- Guermond J.-L., Léorat J., Luddens F., Nore C., 2013, *European Journal of Mechanics-B/Fluids*, 39, 1
- Herreman W., Le Bars M., Le Gal P., 2009, *Physics of Fluids*, 21, 046602
- Herreman W., Cébron D., Le Dizès S., Le Gal P., 2010, *Journal of Fluid Mechanics*, 661, 130
- Hubrig S., et al., 2014, *Astronomy & Astrophysics*, 564, L10
- Hut P., 1981, *Astronomy and Astrophysics*, 99, 126
- Hut P., 1982, *Astronomy and Astrophysics*, 110, 37
- Hypolite D., Mathis S., Rieutord M., 2018, *Astronomy & Astrophysics*, 610, A35
- Ionescu-Kruse D., 2018, *Journal of Mathematical Fluid Mechanics*, 20, 569
- Ivers D., 2017, *Geophysical & Astrophysical Fluid Dynamics*, 111, 333
- Jouve L., Gastine T., Lignières F., 2015, *Astronomy & Astrophysics*, 575, A106
- Kaiser R., Busse F., 2017, *Geophysical & Astrophysical Fluid Dynamics*, 111, 355
- Käpylä P. J., Rheinhardt M., Brandenburg A., Käpylä M. J., 2019, arXiv preprint arXiv:1901.00787
- Kerswell R. R., 1993a, *Geophysical & Astrophysical Fluid Dynamics*, 71, 105
- Kerswell R. R., 1993b, *Geophysical & Astrophysical Fluid Dynamics*, 72, 107
- Kerswell R., 1994, *Journal of Fluid Mechanics*, 274, 219
- Kerswell R. R., 2002, *Annual Review of Fluid Mechanics*, 34, 83
- Kerswell R. R., Malkus W. V. R., 1998, *Geophysical research letters*, 25, 603
- Kippenhahn R., Weigert A., Weiss A., 1990, *Stellar structure and evolution*. Vol. 282, Springer
- Kirillov O. N., Mutabazi I., 2017, *Journal of Fluid Mechanics*, 818, 319
- Kirillov O. N., Stefani F., Fukumoto Y., 2014, *Journal of Fluid Mechanics*, 760, 591
- Kitchatinov L. L., 2014, *The Astrophysical Journal*, 784, 81
- Knobloch E., 1982, *Geophysical & Astrophysical Fluid Dynamics*, 22, 133
- Kochukhov O., Johnston C., Alecian E., Wade G. A., the BinaM-IcS collaboration 2018, *Monthly Notices of the Royal Astronomical Society*, 478, 1749
- Labbé F., Jault D., Gillet N., 2015, *Geophysical & Astrophysical Fluid Dynamics*, 109, 587
- Lacaze L., Le Gal P., Le Dizès S., 2004, *Journal of Fluid Mechanics*, 505, 1
- Lacaze L., Le Gal P., Le Dizès S., 2005, *Physics of the Earth and Planetary Interiors*, 151, 194
- Lacaze L., Ryan K., Le Dizès S., 2007, *Journal of Fluid Mechanics*, 577, 341
- Lai D., Rasio F. A., Shapiro S. L., 1993, *The Astrophysical Journal Supplement Series*, 88, 205
- Landstreet J. D., Kochukhov O., Alecian E., Bailey J. D., Mathis S., Neiner C., Wade G. A., 2017, *Astronomy & Astrophysics*, 601, A129
- Le Bars M., Le Dizès S., 2006, *Journal of Fluid Mechanics*, 563, 189
- Le Bars M., Lacaze L., Le Dizès S., Le Gal P., Rieutord M., 2010, *Physics of the Earth and Planetary Interiors*, 178, 48
- Le Dizès S., 2000, *Physics of Fluids*, 12, 2762
- Le Reun T., Favier B., Barker A. J., Le Bars M., 2017, *Physical Review Letters*, 119, 034502
- Le Reun T., Favier B., Le Bars M., 2018, *Journal of Fluid Mechanics*, 840, 498
- Lebovitz N., Lifschitz A., 1992, *Proceedings of the Royal Society of London A: Mathematical, Physical and Engineering Sciences*, 438, 265
- Lebovitz N. R., Zweibel E., 2004, *The Astrophysical Journal*, 609, 301
- Lehnert B., 1954, *The Astrophysical Journal*, 119, 647
- Lemasquerier D., Grannan A. M., Vidal J., Cébron D., Favier B., Le Bars M., Aurnou J. M., 2017, *Journal of Geophysical Research: Planets*, 122, 1926
- Lifschitz A., 1995, *Physics of Fluids*, 7, 1626
- Lifschitz A., Hameiri E., 1991, *Physics of Fluids*, 3, 2644
- Lifschitz A., Lebovitz N., 1993, *The Astrophysical Journal*, 408, 603
- Lignières F., Petit P., Böhm T., Auriere M., 2009, *Astronomy & Astrophysics*, 500, L41
- Lin Y., Ogilvie G. I., 2017, *Monthly Notices of the Royal Astronomical Society*, 468, 1387
- MacDonald J., Mullan D. J., 2004, *Monthly Notices of the Royal Astronomical Society*, 348, 702
- MacGregor K. B., Cassinelli J. P., 2003, *The Astrophysical Journal*, 586, 480
- Maffioli A., Davidson P. A., 2016, *Journal of Fluid Mechanics*, 786, 210
- Mahy L., Gosset E., Sana H., Damerdji Y., De Becker M., Rauw G., Nitschelm C., 2012, *Astronomy & Astrophysics*, 540, A97
- Makaganik V., et al., 2011, *Astronomy & Astrophysics*, 529, A160
- Malkus W. V. R., 1967, *Journal of Fluid Mechanics*, 28, 793
- Malkus W. V. R., 1989, *Geophysical & Astrophysical Fluid Dynamics*, 48, 123
- Markey P., Tayler R. J., 1973, *Monthly Notices of the Royal Astronomical Society*, 163, 77
- Markey P., Tayler R. J., 1974, *Monthly Notices of the Royal Astronomical Society*, 168, 505
- Marti P., et al., 2014, *Geophysical Journal International*, 197, 119

- Maslov V. P., 1986, *Russian Mathematical Surveys*, 41, 23
- Mathis S., de Brye N., 2011, *Astronomy & Astrophysics*, 526, A65
- Mathis S., Palacios A., Zahn J.-P., 2004, *Astronomy & Astrophysics*, 425, 243
- Mathis S., Neiner C., Minh N. T., 2014, *Astronomy & Astrophysics*, 565, A47
- Mathis S., Prat V., Amard L., Charbonnel C., Palacios A., Lagarde N., Eggenberger P., 2018, *Astronomy & Astrophysics*, 620, A22
- Mathys G., 2017, *Astronomy & Astrophysics*, 601, A14
- Matsui H., et al., 2016, *Geochemistry, Geophysics, Geosystems*, 17, 1586
- Mazeh T., 2008, in Goupil M.-J., Zahn J.-P., Mazeh T., eds., , Vol. 29, *Tidal effects in stars, planets and disks. European Astronomical Society Publications Series*, pp 1–65
- Mirouh G. M., Baruteau C., Rieutord M., Ballot J., 2016, *Journal of Fluid Mechanics*, 800, 213
- Mitchell J. P., Braithwaite J., Reisenegger A., Spruit H., Valdivia J. A., Langer N., 2014, *Monthly Notices of the Royal Astronomical Society*, 447, 1213
- Miyazaki T., 1993, *Physics of Fluids*, 5, 2702
- Miyazaki T., Fukumoto Y., 1991, *Physics of Fluids*, 3, 606
- Miyazaki T., Fukumoto Y., 1992, *Physics of Fluids*, 4, 2515
- Mizerski K. A., Bajer K., 2011, *Physica D: Nonlinear Phenomena*, 240, 1629
- Mizerski K. A., Lyra W., 2012, *Journal of Fluid Mechanics*, 698, 358
- Mizerski K. A., Bajer K., Moffatt H. K., 2012, *Journal of Fluid Mechanics*, 707, 111
- Moffatt H. K., 1978, *Magnetic field generation in electrically conducting fluids. Cambridge University Press*
- Moss D., 2001, in *Magnetic Fields Across the Hertzsprung-Russell Diagram*. p. 305
- Nazarenko S., Kevlahan N. K.-R., Dubrulle B., 1999, *Journal of Fluid Mechanics*, 390, 325
- Nduka A., 1971, *The Astrophysical Journal*, 170, 131
- Nordstrom B., Johansen K. T., 1994, *Astronomy and Astrophysics*, 282, 787
- Ogilvie G. I., 2009, *Monthly Notices of the Royal Astronomical Society*, 396, 794
- Ogilvie G. I., 2014, *Annual Review of Astronomy and Astrophysics*, 52, 171
- Parker E. N., 1979, Oxford, Clarendon Press; New York, Oxford University Press, 1979, 858 p.
- Petit P., et al., 2010, *Astronomy & Astrophysics*, 523, A41
- Petit P., et al., 2011, *Astronomy & Astrophysics*, 532, L13
- Reddy K. S., Favier B., Le Bars M., 2018, *Geophysical Research Letters*, 45, 1741
- Reisenegger A., 2009, *Astronomy & Astrophysics*, 499, 557
- Remus F., Mathis S., Zahn J.-P., 2012, *Astronomy & Astrophysics*, 544, A132
- Rieutord M., 1992, *Astronomy and Astrophysics*, 259, 581
- Rieutord M., 2004, in *Symposium-International Astronomical Union*. pp 394–403
- Rieutord M., 2006, *Astronomy & Astrophysics*, 451, 1025
- Rieutord M., Valdetaro L., 1997, *Journal of Fluid Mechanics*, 341, 77
- Rieutord M., Valdetaro L., 2010, *Journal of Fluid Mechanics*, 643, 363
- Rieutord M., Valdetaro L., 2018, *Journal of Fluid Mechanics*, 844, 597
- Rieutord M., Zahn J.-P., 1997, *The Astrophysical Journal*, 474, 760
- Rieutord M., Georgot B., Valdetaro L., 2000, *Physical review letters*, 85, 4277
- Rincon F., Rieutord M., 2003, *Astronomy & Astrophysics*, 398, 663
- Rocca A., 1987, *Astronomy and Astrophysics*, 175, 81
- Rocca A., 1989, *Astronomy and Astrophysics*, 213, 114
- Rodrigues S. B., 2017, *Journal of Engineering Mathematics*, 106, 1
- Rogers T. M., McElwaine J. N., 2017, *The Astrophysical Journal Letters*, 848, L1
- Rüdiger G., Gellert M., Schultz M., Hollerbach R., Stefani F., 2013, *Monthly Notices of the Royal Astronomical Society*, 438, 271
- Rüdiger G., Gellert M., Spada F., Tereshin I., 2015, *Astronomy & Astrophysics*, 573, A80
- Schaeffer N., 2013, *Geochemistry, Geophysics, Geosystems*, 14, 751
- Schaeffer N., Jault D., Nataf H.-C., Fournier A., 2017, *Geophysical Journal International*, 211, 1
- Schatzman E., 1993, *Astronomy and Astrophysics*, 279, 431
- Schmitt D., 2010, *Geophysical and Astrophysical Fluid Dynamics*, 104, 135
- Schneider F. R. N., Podsiadlowski P., Langer N., Castro N., Fosati L., 2016, *Monthly Notices of the Royal Astronomical Society*, 457, 2355
- Seyed-Mahmoud B., Henderson G., Aldridge K., 2000, *Physics of the Earth and Planetary Interiors*, 117, 51
- Seyed-Mahmoud B., Aldridge K., Henderson G., 2004, *Physics of the Earth and Planetary Interiors*, 142, 257
- Shenar T., et al., 2015, *The Astrophysical Journal*, 809, 135
- Shultz M., Wade G. A., Alecian E., Collaboration B., 2015, *Monthly Notices of the Royal Astronomical Society: Letters*, 454, L1
- Shultz M., Rivinius T., Wade G. A., Alecian E., Petit V., collaboration B., 2017, *Monthly Notices of the Royal Astronomical Society*, 475, 839
- Shultz M. E., Wade G. A., Rivinius T., Neiner C., Alecian E., Bohlender D., Monin D., Sikora J., 2018, *Monthly Notices of the Royal Astronomical Society*, 475, 5144
- Sikora J., Wade G. A., Power J., Neiner C., 2018, *Monthly Notices of the Royal Astronomical Society*, 483, 3127
- Simitev R. D., Busse F. H., 2017, *Geophysical & Astrophysical Fluid Dynamics*, 111, 369
- Spiegel E. A., Veronis G., 1960, *The Astrophysical Journal*, 131, 442
- Spruit H. C., 1999, *Astronomy & Astrophysics*, 349, 189
- Spruit H. C., 2002, *Astronomy & Astrophysics*, 381, 923
- Sreenivasan B., Narasimhan G., 2017, *Journal of Fluid Mechanics*, 828, 867
- Tamajo E., Munari U., Siviero A., Tomasella L., Dallaporta S., 2012, *Astronomy & Astrophysics*, 539, A139
- Taylor R. J., 1973, *Monthly Notices of the Royal Astronomical Society*, 161, 365
- Tennekes H., Lumley J. L., 1972, *A first course in turbulence. MIT Press*
- Townsend A. A., 1958, *Journal of Fluid Mechanics*, 4, 361
- Uytterhoeven K., Harmanec P., Teltng J. H., Aerts C., 2005, *Astronomy & astrophysics*, 440, 249
- Vantighem S., 2014, *Proceedings of the Royal Society of London A: Mathematical, Physical and Engineering Sciences*, 470, 20140093
- Vidal J., Cébron D., 2017, *Journal of Fluid Mechanics*, 833, 469
- Vidal J., Schaeffer N., 2015, *Geophysical Journal International*, 202, 2182
- Vidal J., Cébron D., Schaeffer N., 2016, in *19eme Rencontre du Non-Linéaire*.
- Vidal J., Cébron D., Schaeffer N., Hollerbach R., 2018, *Monthly Notices of the Royal Astronomical Society*, 475, 4579
- Wade G. A., et al., 2015, *Monthly Notices of the Royal Astronomical Society*, 456, 2
- Waite M. L., Bartello P., 2006, *Journal of Fluid Mechanics*, 568, 89
- Witte M. G., Savonije G. J., 1999, *Astronomy and Astrophysics*,

- 350, 129
 Witte M. G., Savonije G. J., 2001, *Astronomy & Astrophysics*, 366, 840
 Zahn J.-P., 1966, *Annales d’Astrophysique*, 29, 313
 Zahn J.-P., 1974, in *Symposium-International Astronomical Union*. pp 185–195
 Zahn J.-P., 1975, *Astronomy and Astrophysics*, 41, 329
 Zahn J.-P., 1977, *Astronomy and Astrophysics*, 57, 383
 Zahn J.-P., 1992, *Astronomy and Astrophysics*, 265, 115
 Zahn J.-P., 2008, *Proceedings of the International Astronomical Union*, 4, 47
 Zhang K., 1993, *Journal of Fluid Mechanics*, 248, 203
 Zhang K., Liao X., Schubert G., 2003, *The Astrophysical Journal*, 585, 1124
 Zimmerman M. K., Thompson S. E., Mullally F., Fuller J., Shporer A., Hambleton K., 2017, *The Astrophysical Journal*, 846, 147

APPENDIX A: MAC MODES IN TRIAXIAL ELLIPSOIDS

In this appendix, we present a new method to compute the three-dimensional hydromagnetic eigenmodes of an stratified Boussinesq fluid contained within a rigid triaxial ellipsoid. This approach relies on a fully global, explicit spectral method in ellipsoids, in which the velocity field is described by polynomial finite-dimensional Galerkin bases. The algorithm has been implemented within the new code SHINE (<https://bitbucket.org/vidalje/shine>). It has been benchmarked successfully for the Coriolis modes in ellipsoids (Vantieghem 2014; Lemasquerier et al. 2017), while the fast and slow hydromagnetic solutions have been validated for the Malkus field in spheres (Malkus 1967; Zhang et al. 2003), spheroids (Kerswell 1994) and triaxial ellipsoids (Vidal et al. 2016).

A1 Assumptions

We work in dimensional variables for the sake of generality, and use the notations introduced in the main text. We consider a diffusionless, incompressible electrically conducting fluid, contained within a triaxial ellipsoid of semi-axes (a, b, c) . The fluid is stratified under the gravity field \mathbf{g}^* in the Boussinesq approximation. The fluid is contained within an ellipsoidal container, which is rotating at the angular velocity $\boldsymbol{\Omega}$ in the inertial frame. We expand the velocity, the temperature and the magnetic field as small perturbations $[\mathbf{u}^*, \Theta^*, \mathbf{b}^*](\mathbf{r}, t)$ around an equilibrium state of rest $[\mathbf{0}, T_0^*, \mathbf{B}_0^*](\mathbf{r})$.

In the linear approximation, the dimensional governing equations are

$$\frac{\partial \mathbf{u}^*}{\partial t} = -2\boldsymbol{\Omega} \times \mathbf{u}^* - \nabla p^* - \alpha_T \Theta^* \mathbf{g}^* + \alpha_B [(\nabla \times \mathbf{b}^*) \times \mathbf{B}_0^* + (\nabla \times \mathbf{B}_0^*) \times \mathbf{b}^*], \quad (\text{A1a})$$

$$\frac{\partial \Theta^*}{\partial t} = -(\mathbf{u}^* \cdot \nabla) T_0^*, \quad (\text{A1b})$$

$$\frac{\partial \mathbf{b}^*}{\partial t} = \nabla \times (\mathbf{u}^* \times \mathbf{B}_0^*), \quad (\text{A1c})$$

$$\nabla \cdot \mathbf{u}^* = \nabla \cdot \mathbf{b}^* = 0, \quad (\text{A1d})$$

with $\alpha_B = (\rho_M \mu_0)^{-1}$ and p^* the hydrodynamic pressure. By

taking the time derivative of equations (A1), we can obtain a single wave-like equation of second order in time for the velocity perturbation \mathbf{u}^* . This reads

$$\frac{\partial^2 \mathbf{u}^*}{\partial t^2} + 2\boldsymbol{\Omega} \times \frac{\partial \mathbf{u}^*}{\partial t} = -\frac{\partial \nabla p^*}{\partial t} + \alpha_T (\mathbf{u}^* \cdot \nabla) T_0^* \mathbf{g}^* + \mathbf{f}_m^*, \quad (\text{A2})$$

with the Lorentz force

$$\mathbf{f}_m^* = \alpha_B (\nabla \times \mathbf{B}_0^*) \times [\nabla \times (\mathbf{u}^* \times \mathbf{B}_0^*)] + \alpha_B [\nabla \times (\nabla \times (\mathbf{u}^* \times \mathbf{B}_0^*))] \times \mathbf{B}_0^*. \quad (\text{A3})$$

Note that equations (A1) cannot be recast into a single equation for the velocity perturbation \mathbf{u}^* in the presence of an arbitrary basic flow \mathbf{U}_0^* , e.g. flow (7) considered in the main text. However, we point out that some well-chosen ellipsoidal equilibrium configurations may be reduced to a single equation (e.g. in spheres Friedlander 1989).

Finally, equation (A2) is supplemented by the non-penetration boundary conditions

$$\mathbf{u}^* \cdot \mathbf{1}_n = 0, \quad \mathbf{B}_0^* \cdot \mathbf{1}_n = 0. \quad (\text{A4})$$

with $\mathbf{1}_n$ the unit outward vector normal to the ellipsoidal boundary. We emphasise that alternative boundary conditions for the background magnetic field cannot be considered, at least to investigate consistently all the hydromagnetic modes. Indeed, allowing a non-zero normal magnetic field at the boundary would create a surface electrical density current generating a Lorentz force \mathbf{f}_m^* in the form of a discontinuous Dirac function distributed on the boundary (Friedlander & Vishik 1990). This would lead to spurious diffusionless solutions for the slow hydromagnetic modes. However, we would expect the fast hydromagnetic modes to be only barely affected by the magnetic boundary condition, since the Lorentz force in momentum equation (A2) has only second-order effects on the fast modes.

A2 Galerkin method

We employ the method of Galerkin weighted residuals (e.g. Finlayson 2013) to describe the velocity field. We seek a finite-dimensional Galerkin expansion of the modes as

$$[\mathbf{u}^*, p^*](\mathbf{r}, t) = [\widehat{\mathbf{u}}^*, \widehat{p}^*](\mathbf{r}) \exp(i\omega_i t), \quad \widehat{\mathbf{u}}^* = \sum_{l=1}^{\infty} \gamma_l \widehat{\mathbf{u}}_l^*, \quad (\text{A5})$$

where ω_i is the angular frequency, $\{\gamma_l\}$ modal complex coefficients and $\{\widehat{\mathbf{u}}_l(\mathbf{r})\}$ real basis Galerkin elements (see later). Then, we rewrite equation (A2) in the symbolic form

$$\left(-\omega_i^2 \mathcal{A}_2 + i\omega_i \mathcal{A}_1 + \mathcal{A}_0\right) \widehat{\mathbf{u}}^* = i\omega_i \nabla \widehat{p}^*, \quad (\text{A6})$$

where $[\mathcal{A}_2, \mathcal{A}_1, \mathcal{A}_0]$ are three linear operators.

The basis elements $\{\widehat{\mathbf{u}}_l(\mathbf{r})\}$ are made of linear combinations of Cartesian monomials $\{x^i y^j z^k\}_{i+j+k < \infty}$ satisfying

$$\nabla \cdot \widehat{\mathbf{u}}_l^* = 0, \quad \widehat{\mathbf{u}}_l^* \cdot \mathbf{1}_n = 0. \quad (\text{A7})$$

Expansion (A5) is similar to expansions used in the finite-element method (FEM). However, compared to the traditional FEM, our basis elements $\{\widehat{\mathbf{u}}_l(\mathbf{r})\}$ are global polynomials, infinitely continuously differentiable in ellipsoids. The mathematical completeness of the polynomial expansion for incompressible fluids is then ensured by using the

Weierstrass approximation theorem (Backus & Rieutord 2017; Ivers 2017). Hence, this method is a rigorous spectral method in ellipsoids. Several Cartesian expansions have been proposed, see a comparison in Vidal & Cébron (2017).

Then, we truncate the series (A5) at a given polynomial degree n such that $i + j + k \leq n$. In the absence of any stratified or magnetic effect, the Coriolis operator is exactly closed within the considered polynomial bases $i + j + k \leq n$ (e.g. Kerswell 1993b; Backus & Rieutord 2017). Thus, the Coriolis modes are exactly described by these polynomial bases (see computations in Vantieghem 2014; Lemasquerier et al. 2017). Note that fast and slow MC modes also admit exact polynomial descriptions for background magnetic fields which are linear in the Cartesian space coordinates (Malkus 1967; Vidal et al. 2016). For any other practical configuration, we have to choose a maximum polynomial degree n to ensure a good enough convergence of the desired modes (since higher order bases are excited by the buoyancy and Lorentz forces). We substitute the truncated expansion into equation (A6), yielding the quadratic eigenvalue problem

$$\left(-\omega_i^2 \mathbf{A}_2 + i\omega_i \mathbf{A}_1 + \mathbf{A}_0\right) \boldsymbol{\gamma} = \mathbf{0}, \quad (\text{A8})$$

where $\boldsymbol{\gamma} = (\gamma_1, \gamma_2, \dots)^\top$ is the eigenvector and $[\mathbf{A}_2, \mathbf{A}_1, \mathbf{A}_0]$ are three matrices. Their elements are given by the Galerkin projections over the ellipsoidal domain

$$A_{2,ij} = \int_{\mathcal{V}} \widehat{\mathbf{u}}_i^* \cdot \mathcal{A}_2 \widehat{\mathbf{u}}_j^* d\mathcal{V}, \quad (\text{A9a})$$

$$A_{1,ij} = \int_{\mathcal{V}} \widehat{\mathbf{u}}_i^* \cdot \mathcal{A}_1 \widehat{\mathbf{u}}_j^* d\mathcal{V}, \quad (\text{A9b})$$

$$A_{0,ij} = \int_{\mathcal{V}} \widehat{\mathbf{u}}_i^* \cdot \mathcal{A}_0 \widehat{\mathbf{u}}_j^* d\mathcal{V}. \quad (\text{A9c})$$

The volume integral for a given Cartesian monomial $x^i y^j z^k$ is exactly given by

$$\int_{\mathcal{V}} x^i y^j z^k d\mathcal{V} = \frac{2a^{i+1} b^{j+1} c^{k+1}}{3+i+j+k} \beta\left(\frac{i+j}{2} + 1, \frac{k+1}{2}\right) \times \beta\left(\frac{i+1}{2}, \frac{j+1}{2}\right) \quad (\text{A10})$$

if $[i, j, k]$ are all even and vanishes otherwise, where $\beta(i, j)$ is the transcendental beta function defined as a function of the Gamma function $\Gamma(i)$ by

$$\beta(i, j) = \frac{\Gamma(i)\Gamma(j)}{\Gamma(i+j)}, \quad \Gamma\left(i + \frac{1}{2}\right) = \frac{(2i)!}{2^{2i} i!} \sqrt{\pi}. \quad (\text{A11})$$

Note that the pressure term vanishes in equation (A8) by virtue of the divergence theorem, such that an explicit decomposition for the pressure is not required.

APPENDIX B: ECCENTRIC, SYNCHRONISED ORBITS

In this appendix, we consider synchronous stratified binary systems moving on weakly eccentric coplanar orbits. Note that the following results are also relevant for stratified moons or gaseous planets orbiting around a massive central body (e.g. Kerswell & Malkus 1998; Cébron et al. 2012b;

Lemasquerier et al. 2017). We consider a diffusionless tidal model of the tidally deformed fluid body, characterised by an equatorial ellipticity β_0 . The fluid body is rotating at the uniform angular velocity Ω_s , aligned in the inertial frame with the orbital angular velocity of the companion along $\mathbf{1}_z$. We use the dimensionless variables introduced in §2, i.e. taking $(\Omega_s)^{-1}$ as the relevant time scale. Due to the weak orbital eccentricity $e \ll 1$, the orbital angular velocity has periodic time variations. For the sake of generality, we assume that the tidal forcing has the following (dimensionless) expression, at the leading order in the eccentricity,

$$\Omega_0(t) = 1 + \epsilon \cos(ft). \quad (\text{B1})$$

where f is the dimensionless frequency of the forcing and $\epsilon \leq 2e$ their dimensionless amplitude. Forcing (B1) is known as longitudinal librations. For this tidal forcing, the equilibrium tide velocity field has the following form in the central frame

$$U_0(\mathbf{r}, t) = -2\epsilon \left[-(1 + \beta_0)y \mathbf{1}_x + (1 - \beta_0)x \mathbf{1}_y \right]. \quad (\text{B2})$$

The above tidal flow (B2) is prone to the libration-driven tidal instability, which is quite similar to the tidal instability in non-synchronised systems (e.g. Kerswell & Malkus 1998; Cébron et al. 2012b; Vidal & Cébron 2017). Indeed, this fluid instability is due to a sub-harmonic resonance between two waves of angular frequency $|\omega_i|$ interacting the basic flow (B2). By analogy with formula (9) in non-synchronised systems, the sub-harmonic resonant condition yields

$$|\omega_i| = f/4. \quad (\text{B3})$$

The four kinds of waves $[\mathcal{H}_1, \mathcal{H}_2, \mathcal{E}_1, \mathcal{E}_2]$, introduced §3.3, are involved in the instability mechanism. We show the nature of the waves satisfying condition (B3) in figure B1. The classical allowable range of the instability is $0 \leq f \leq 4$ (e.g. Cébron et al. 2012a), in which only triadic couplings of inertia-gravity waves $[\mathcal{H}_1, \mathcal{H}_2, \mathcal{E}_1]$ are involved. In this frequency range, the instability is trapped along critical latitudes for a strong enough stratification, i.e. when $N_0/\Omega_s \gg 1$. Similar to the non-synchronised configurations, it turns out that the largest growth rate is unaffected by the ratio N_0/Ω_s on these critical latitude. Thus, they are predicted by the diffusionless formula obtained in neutral fluids (see formula 4 of Cébron et al. 2012a).

In the other frequency range $f > 4$, the instability is only due to triadic couplings of internal-gravity waves $[\mathcal{E}_1, \mathcal{E}_2]$ modified by the rotation. Moreover, the instability only exists for strong enough stratification $N_0/\Omega_s \gg 1$.

Finally, we can use a mixing-length theory to get a phenomenological prescription of the tidal mixing, by similar analogy with non-synchronised orbits. The main difference with non-synchronised systems is that the typical turbulent velocity u_t should scale as (Favier et al. 2015; Grannan et al. 2016)

$$u_t \sim \epsilon \beta_0 R \Omega_s. \quad (\text{B4})$$

Hence, the turbulent time scale for the tidal disruption of the fossil field (45) ought to be reduced in synchronised systems, yielding the prescription

$$\tau_t \propto \frac{1}{\epsilon^2 \beta_0^2 \Omega_s}. \quad (\text{B5})$$

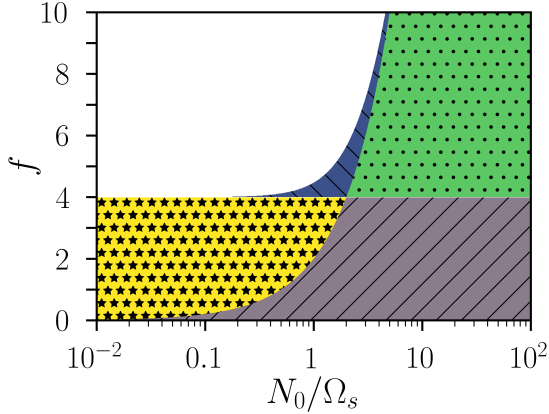


Figure B1. Waves at the sub-harmonic resonance condition (B3) for synchronised systems, as a function of the (dimensionless) forcing frequency f and N_0/Ω_s . The other notations are identical to the ones introduced in the main text. White regions: no compatible waves satisfying (B3). Stars (yellow area): hyperbolic waves \mathcal{H}_1 . Right slash (purple area): hyperbolic waves \mathcal{H}_2 . Dots (green area): elliptic waves \mathcal{E}_1 . Back slash (blue area): elliptic waves \mathcal{E}_2 . The classical allowable region of the instability is $0 \leq f \leq 4$ in neutral fluids.

APPENDIX C: LOCAL (WKB) STABILITY EQUATIONS

In this appendix, we present the local Wentzel-Kramers-Brillouin (WKB) stability method. In the local analysis, the unbounded growth of the perturbations gives sufficient conditions for local instability (Friedlander & Vishik 1991; Lifschitz & Hameiri 1991). The original WKB hydrodynamic stability theory has been extended by several authors, e.g. to take into account thermal effects within the Boussinesq approximation (Kirillov & Mutabazi 2017). The theory has also been rediscovered in atmospheric sciences and oceanography (e.g. Ionescu-Kruse 2018).

In the following, we derive the coupled (WKB) stability equations for arbitrary, spatially varying Boussinesq and magnetic background states. We emphasise that their derivation is intrinsically different from the one of Kelvin wave stability equations (Craik & Criminale 1986; Craik 1989), also accounting for magnetic fields (Craik 1988; Fabijonas 2002; Lebovitz & Zweibel 2004; Herreman et al. 2009; Mizerski & Bajer 2011; Cébron et al. 2012b; Mizerski et al. 2012; Mizerski & Lyra 2012; Bajer & Mizerski 2013) and buoyancy effects (Cébron et al. 2012b). Indeed, the Kelvin wave method cannot investigate the stability of arbitrary background states, contrary to the WKB method. In addition, we have also extended the stability theory to consistently account for two transport scalar equations, e.g. governing temperature and chemical composition that diffuse at very different rates in stellar interiors. These double-diffusive, hydromagnetic stability equations may be relevant to investigate other local instabilities in stratified interiors, e.g. the GSF instability in differentially rotating bodies (Goldreich & Schubert 1967; Knobloch 1982).

C1 Linearised stability equations

We use in the following dimensional variables to devise the general stability equations. Contrary to the main text, the dimensional variables are written here without $*$, to keep concise mathematical expressions. We consider a fluid rotating at the angular velocity $\mathbf{\Omega}$ and stratified in density under the arbitrary gravity field \mathbf{g} . The fluid has a typical density ρ_* , a kinematic viscosity ν , a magnetic diffusivity η , a thermal diffusivity κ_T and a compositional diffusivity κ_C . The fluid is also pervaded by an imposed magnetic field $\mathbf{B}_0(\mathbf{r}, t)$. We expand the velocity, the magnetic field, the temperature and the composition (in light elements) as small Eulerian perturbations $[\mathbf{u}, \mathbf{b}, \Theta, \xi](\mathbf{r}, t)$ around a spatially varying and time-dependent background state $[\mathbf{U}_0, \mathbf{B}_0, T_0, C_0](\mathbf{r}, t)$. In unbounded fluids, the perturbations are governed by the linearised hydromagnetic, double-diffusive Boussinesq equations

$$\frac{d\mathbf{u}}{dt} = -(\mathbf{u} \cdot \nabla) \mathbf{U}_0 - 2\mathbf{\Omega} \times \mathbf{u} - \nabla(p + p_b) + \nu \nabla^2 \mathbf{u} - (\alpha_T \Theta + \alpha_C \xi) \mathbf{g} + \alpha_B (\mathbf{B}_0 \cdot \nabla \mathbf{b} + \mathbf{b} \cdot \nabla \mathbf{B}_0), \quad (\text{C1a})$$

$$\frac{d\mathbf{b}}{dt} = \mathbf{b} \cdot \nabla \mathbf{U}_0 - (\mathbf{u} \cdot \nabla) \mathbf{B}_0 + (\mathbf{B}_0 \cdot \nabla) \mathbf{u} + \eta \nabla^2 \mathbf{b}, \quad (\text{C1b})$$

$$\frac{d\Theta}{dt} = -(\mathbf{u} \cdot \nabla) T_0 + \kappa_T \nabla^2 \Theta, \quad (\text{C1c})$$

$$\frac{d\xi}{dt} = -(\mathbf{u} \cdot \nabla) C_0 + \kappa_C \nabla^2 \xi, \quad (\text{C1d})$$

$$\nabla \cdot \mathbf{u} = 0, \quad \nabla \cdot \mathbf{b} = 0, \quad (\text{C1e})$$

where $d/dt = \partial/\partial t + (\mathbf{U}_0 \cdot \nabla)$ is the material derivative along the basic flow, p is the hydrodynamic pressure and $p_b = \alpha_B (\mathbf{B}_0 \cdot \mathbf{b})$ the magnetic pressure. In equations (C1), (α_T, α_C) are the coefficients of thermal and compositional expansion (at constant pressure) in the Boussinesq equation of state (EoS)

$$\delta\rho = \rho_*(1 - \alpha_T \Theta - \alpha_C \xi) \quad (\text{C2})$$

with $\delta\rho$ the Eulerian perturbation in density. By considering the composition in light elements, buoyancy effects are symmetrical in EoS (C2) and in momentum equation (C1a).

C2 Eulerian stability equations

C2.1 Short-wavelength perturbations

We seek short-wavelength perturbations in Eulerian description, with respect to the small asymptotic parameter $0 < \varepsilon \ll 1$. We introduce the formal asymptotic series

$$\mathbf{u}(\mathbf{r}, t) = \left[\mathbf{u}^{(0)} + \varepsilon \mathbf{u}^{(1)} \right] (\mathbf{r}, t) \exp(i\Phi(\mathbf{r}, t)/\varepsilon) + \dots, \quad (\text{C3a})$$

$$\mathbf{b}(\mathbf{r}, t) = \left[\mathbf{b}^{(0)} + \varepsilon \mathbf{b}^{(1)} \right] (\mathbf{r}, t) \exp(i\Phi(\mathbf{r}, t)/\varepsilon) + \dots, \quad (\text{C3b})$$

$$\Theta(\mathbf{r}, t) = \left[\Theta^{(0)} + \varepsilon \Theta^{(1)} \right] (\mathbf{r}, t) \exp(i\Phi(\mathbf{r}, t)/\varepsilon) + \dots, \quad (\text{C3c})$$

$$\xi(\mathbf{r}, t) = \left[\xi^{(0)} + \varepsilon \xi^{(1)} \right] (\mathbf{r}, t) \exp(i\Phi(\mathbf{r}, t)/\varepsilon) + \dots, \quad (\text{C3d})$$

$$p(\mathbf{r}, t) = \left[p^{(0)} + \varepsilon p^{(1)} \right] (\mathbf{r}, t) \exp(i\Phi(\mathbf{r}, t)/\varepsilon) + \dots, \quad (\text{C3e})$$

where Φ is a real-valued scalar function that represents the rapidly varying phase of oscillations and $[\mathbf{u}^{(i)}, \Theta^{(i)}, \xi^{(i)}, p^{(i)}]$ are slowly varying complex-valued amplitudes. Note that we

have omitted in expansions (C3) the reminder terms, assumed to be uniformly bounded in ε on any fixed time interval (Lifschitz & Hameiri 1991; Lebovitz & Lifschitz 1992; Lifschitz & Lebovitz 1993). We further introduce the local wave vector, defined by $\mathbf{k} = \nabla\Phi$. The small asymptotic parameter $\varepsilon \ll 1$ is actually related to the typical scale of the instability l , which must be much smaller to the typical length scale of the large-scale background flow L_0 . This yields (Nazarenko et al. 1999) $\varepsilon = l/L_0 \ll 1$. In the hydrodynamic and diffusionless case, its value is arbitrary small.

However, in hydromagnetics, ε does depend on the magnetic field, since the Lorentz force does depend on the length scale. The general magnetic configuration leads to a set of partial differential equations (Friedlander & Vishik 1995; Kirillov et al. 2014), which must be solved locally in Eulerian description. However, by assuming (see also for uniform fields Mizerski & Bajer 2011)

$$\mathbf{B}_0(\mathbf{r}) = \varepsilon \widetilde{\mathbf{B}}_0(\mathbf{r}), \quad (\text{C4})$$

the partial differential equations simplify into ordinary differential equations (even for spatially varying magnetic fields). This is the central approximation of the theory. In dimensionless form, we may assume that the background field has a typical dimensionless amplitude $Le \ll 1$, yielding $\varepsilon = Le$.

C2.2 Diffusionless equations

We closely follow the mathematical derivation of Kirillov & Mutabazi (2017), extending it to the hydromagnetic case. Substituting expansions (C3) in incompressible condition (C1e) and collecting terms of order i/ε^{-1} and ε^0 yields

$$i/\varepsilon^{-1} : \left[\mathbf{u}^{(0)}, \mathbf{b}^{(0)} \right] \cdot \mathbf{k} = 0, \quad (\text{C5a})$$

$$\varepsilon^0 : \nabla \cdot \left[\mathbf{u}^{(0)}, \mathbf{b}^{(0)} \right] = -i\mathbf{k} \cdot \left[\mathbf{u}^{(1)}, \mathbf{b}^{(1)} \right]. \quad (\text{C5b})$$

The same procedure applied to governing equations (C1a)-(C1d). First, it yields at the order i/ε^{-1}

$$\frac{d\Phi}{dt} \left[\mathbf{u}^{(0)}, \mathbf{b}^{(0)}, \Theta^{(0)}, \xi^{(0)} \right] = \left[-p^{(0)}\mathbf{k}, \mathbf{0}, \mathbf{0}, 0 \right]. \quad (\text{C6})$$

The dot product of the first equation (C6) with $\nabla\Phi$, under constraint (C5a), yields $p^{(0)} = 0$. Then, we obtain the Hamilton-Jacobi equation

$$\frac{d\Phi}{dt} = 0. \quad (\text{C7})$$

Finally, taking the spatial gradient of equation (C7) reads the eikonal equation together with its initial condition (Lifschitz & Hameiri 1991)

$$\frac{d\mathbf{k}}{dt} = -(\nabla U_0)^\top \mathbf{k}, \quad \mathbf{k}(\mathbf{r}, 0) = \mathbf{k}_0, \quad |\mathbf{k}(\mathbf{r}, t)| = |\mathbf{k}_0|. \quad (\text{C8})$$

Now, by using (C7) and (C8), equations (C1a)-(C1d)

yield at the next asymptotic order ε^0

$$-i\mathbf{k} \left[p^{(1)} + \alpha_B \widetilde{\mathbf{B}}_0 \cdot \mathbf{b}^{(0)} \right] = \left(\frac{d}{dt} + \nabla U_0 + 2\boldsymbol{\Omega} \times \right) \mathbf{u}^{(0)} \quad (\text{C9a})$$

$$- \left(\alpha_T \Theta^{(0)} + \alpha_C \xi^{(0)} \right) \mathbf{g} - i\alpha_B (\widetilde{\mathbf{B}}_0 \cdot \mathbf{k}) \mathbf{b}^{(0)},$$

$$\frac{d\mathbf{b}^{(0)}}{dt} = i(\widetilde{\mathbf{B}}_0 \cdot \mathbf{k}) \mathbf{u}^{(0)} + (\nabla U_0) \mathbf{b}^{(0)}, \quad (\text{C9b})$$

$$\frac{d\Theta^{(0)}}{dt} = -\mathbf{u}^{(0)} \cdot \nabla T_0, \quad (\text{C9c})$$

$$\frac{d\xi^{(0)}}{dt} = -\mathbf{u}^{(0)} \cdot \nabla C_0. \quad (\text{C9d})$$

Equations (C9b)-(C9d) are transport equations for the magnetic field, the temperature and the composition amplitudes. Applying the dot product of \mathbf{k} with equation (C9a) gives the first order pressure variable

$$-i \left[p^{(1)} + \alpha_B \widetilde{\mathbf{B}}_0 \cdot \mathbf{b}^{(0)} \right] = \frac{\mathbf{k}}{|\mathbf{k}|^2} \cdot \left(\frac{d}{dt} + \nabla U_0 + 2\boldsymbol{\Omega} \times \right) \mathbf{u}^{(0)} - \frac{\mathbf{k}}{|\mathbf{k}|^2} \cdot \left(\alpha_T \Theta^{(0)} + \alpha_C \xi^{(0)} \right) \mathbf{g}, \quad (\text{C10})$$

Then, we differentiate equation (C5a) to get the identity (Lifschitz & Hameiri 1991)

$$\frac{d}{dt} (\mathbf{u}^{(0)} \cdot \mathbf{k}) = \frac{d\mathbf{k}}{dt} \cdot \mathbf{u}^{(0)} + \mathbf{k} \cdot \frac{d\mathbf{u}^{(0)}}{dt} = 0. \quad (\text{C11})$$

Finally, we use identity (C11) to simplify equation (C10), then we substitute the resulting expression into equation (C9a). After some algebra, we get the transport equation for the velocity amplitude

$$\frac{d\mathbf{u}^{(0)}}{dt} = \left[\left(\frac{2\mathbf{k}\mathbf{k}^\top}{|\mathbf{k}|^2} - \mathbf{I} \right) \nabla U_0 + 2 \left(\frac{\mathbf{k}\mathbf{k}^\top}{|\mathbf{k}|^2} - \mathbf{I} \right) \boldsymbol{\Omega} \times \right] \mathbf{u}^{(0)} - \left(\mathbf{I} - \frac{\mathbf{k}\mathbf{k}^\top}{|\mathbf{k}|^2} \right) \mathbf{g} \left(\alpha_T \Theta^{(0)} + \alpha_C \xi^{(0)} \right) + i\alpha_B (\widetilde{\mathbf{B}}_0 \cdot \mathbf{k}) \mathbf{b}^{(0)}. \quad (\text{C12})$$

The stability equations, given by equations (C12) and (C9b)-(C9d), are dominant for the stability behaviour of WKB expansions (C3) for long enough times in the limit $\varepsilon \ll 1$ (Lifschitz & Hameiri 1991; Friedlander & Vishik 1991; Lebovitz & Lifschitz 1992; Lifschitz & Lebovitz 1993). The next order terms are only responsible for transient behaviours (Rodrigues 2017). Thus, sufficient conditions for local instability are obtained by solving transport equations (C12) and (C9b)-(C9d).

C2.3 Diffusive effects

Extending the diffusionless WKB equations to the diffusive regime is subtle. For instance, the diffusive term $\nu \nabla^2 \mathbf{u}$ is written as (Kirillov et al. 2014)

$$\nabla^2 \mathbf{u} = \exp\left(\frac{i\Phi}{\varepsilon}\right) \left(\nabla^2 + i\frac{2}{\varepsilon}(\mathbf{k} \cdot \nabla) + \frac{i}{\varepsilon} \nabla^2 \Phi - \frac{|\mathbf{k}|^2}{\varepsilon^2} \right) \left(\mathbf{u}^{(0)} + \varepsilon \mathbf{u}^{(1)} \right) + \dots \quad (\text{C13})$$

As first noticed by Maslov (1986), Lifschitz & Hameiri (1991) and Lifschitz & Lebovitz (1993), formula (C13) shows that the WKB ansatz $\exp(i\Phi/\varepsilon)$ quickly dies out because of diffusion, unless ε has a quadratic dependence on the diffusion

coefficients. Hence, we must rescale the dimensional diffusivities as

$$[\nu, \eta, \kappa_T, \kappa_C,] = \varepsilon^2 [\tilde{\nu}, \tilde{\eta}, \tilde{\kappa}_T, \tilde{\kappa}_C], \quad (\text{C14})$$

e.g. with $\varepsilon = Le$ in the dimensionless hydromagnetic case. Then, the diffusionless equations are augmented by included in the right-hand sides the leading-order diffusive terms $[-\tilde{\nu}|\mathbf{k}|^2\mathbf{u}^{(0)}, -\tilde{\eta}|\mathbf{k}|^2\mathbf{b}^{(0)} - \tilde{\kappa}_T|\mathbf{k}|^2\Theta^{(0)}, -\tilde{\kappa}_C|\mathbf{k}|^2\xi^{(0)}]$.

C3 Lagrangian equations along fluid trajectories

WKB stability equations are partial differential equations in Eulerian description. However, they are generally solved in Lagrangian description. The WKB perturbations are advected along the fluid trajectories $\mathbf{X}(t)$ of the background flow \mathbf{U}_0 , passing through the initial point \mathbf{X}_0 at initial time $t = 0$. In Lagrangian formalism, the double-diffusive WKB stability equations are

$$\frac{D\mathbf{X}}{Dt} = \mathbf{U}_0(\mathbf{X}(t)), \quad \mathbf{X}(0) = \mathbf{X}_0, \quad (\text{C15a})$$

$$\frac{D\mathbf{k}}{Dt} = -(\nabla\mathbf{U}_0)^\top \mathbf{k}, \quad \mathbf{k}(0) = \mathbf{k}_0, \quad (\text{C15b})$$

$$\frac{D\mathbf{u}^{(0)}}{Dt} = \left[\left(\frac{2\mathbf{k}\mathbf{k}^\top}{|\mathbf{k}|^2} - \mathbf{I} \right) \nabla\mathbf{U}_0 + 2 \left(\frac{\mathbf{k}\mathbf{k}^\top}{|\mathbf{k}|^2} - \mathbf{I} \right) \boldsymbol{\Omega} \times \right] \mathbf{u}^{(0)} \quad (\text{C15c})$$

$$-\tilde{\nu}|\mathbf{k}|^2 - \left(\mathbf{I} - \frac{\mathbf{k}\mathbf{k}^\top}{|\mathbf{k}|^2} \right) \mathbf{g} \left(\alpha_T \Theta^{(0)} + \alpha_C \xi^{(0)} \right) + i\alpha_B(\tilde{\mathbf{B}}_0 \cdot \mathbf{k}) \mathbf{b}^{(0)},$$

$$\frac{D\mathbf{b}^{(0)}}{Dt} = i(\tilde{\mathbf{B}}_0 \cdot \mathbf{k}) \mathbf{u}^{(0)} + (\nabla\mathbf{U}_0) \mathbf{b}^{(0)} - \tilde{\eta}|\mathbf{k}|^2\mathbf{b}^{(0)}, \quad (\text{C15d})$$

$$\frac{D\Theta^{(0)}}{Dt} = -\mathbf{u}^{(0)} \cdot \nabla T_0 - \tilde{\kappa}_T|\mathbf{k}|^2\Theta^{(0)}, \quad (\text{C15e})$$

$$\frac{D\xi^{(0)}}{Dt} = -\mathbf{u}^{(0)} \cdot \nabla C_0 - \tilde{\kappa}_C|\mathbf{k}|^2\Theta^{(0)}, \quad (\text{C15f})$$

with D/Dt the Lagrangian derivative. Therefore, equations (C15) are interpreted as ordinary differential equations along the fluid trajectories of the background flow \mathbf{U}_0 for the amplitudes $(\mathbf{u}^{(0)}, \Theta^{(0)}, \xi^{(0)})$. In addition, the initial conditions satisfy

$$\mathbf{u}^{(0)}(0) \cdot \mathbf{k}_0 = 0, \quad \mathbf{b}^{(0)}(0) \cdot \mathbf{k}_0 = 0, \quad (\text{C16})$$

such the solenoidal conditions for the velocity and the magnetic field hold at any time. Sufficient conditions for instability are obtained when (e.g. Lifschitz & Hameiri 1991; Lebovitz & Lifschitz 1992; Lifschitz & Lebovitz 1993)

$$\lim_{t \rightarrow \infty} \left(|\mathbf{u}^{(0)}| + |\mathbf{b}^{(0)}| + |\Theta^{(0)}| + |\xi^{(0)}| \right) = \infty \quad (\text{C17})$$

for given $[\mathbf{X}_0, \mathbf{k}_0]$ and with suitable initial conditions for $[\mathbf{u}^{(0)}, \mathbf{b}^{(0)}, \Theta^{(0)}, \xi^{(0)}]$.

APPENDIX D: MIXED RESONANCES OF SLOW/FAST WAVES

In this appendix, we show that the mixed couplings between slow and fast hydromagnetic waves can be discarded in resonance condition (8). We use the same dimensionless variables as in the main text. In the regime $Le \ll 1$, Kerswell (1993a, 1994) obtained that the typical diffusionless growth rate of

the tidal instability involving mixed couplings scales as (in dimensionless form)

$$\sigma \propto Le^4 \beta_0. \quad (\text{D1})$$

This diffusionless growth rate must be larger than the Joule damping rate of the slow waves, which is $\tau_\Omega \propto -Em|\mathbf{k}_0|^2$ in the local theory (Rincon & Rieutord 2003; Sreenivasan & Narasimhan 2017). This gives the typical upper bound on the wave vector

$$|\mathbf{k}_0|^2 \ll \frac{Le^4}{Em} \beta_0. \quad (\text{D2})$$

In short-period binaries, the typical value for the equatorial ellipticity is $\beta_0 \sim 10^{-2}$ (see table 2). As given in table 1, we have also the typical numbers $Em \leq 10^{-10}$ and $Le \leq 10^{-5}$. Then, condition (D2) yields the upper bound $|\mathbf{k}_0| \ll 1$. This is incompatible with the short-wavelength stability theory, which requires $|\mathbf{k}_0| \gg 1$. Physically, this shows that the Joule damping rate is always larger than the diffusionless growth rate in non-ideal fluids, for any resonance involving slow MC waves in the regime $Le \ll 1$. Therefore, mixed couplings of fast/slow waves can be discarded for the tidal instability in realistic stellar interiors.

This paper has been typeset from a $\text{\TeX}/\text{\LaTeX}$ file prepared by the author.